

# **Olivine trace element geochemistry of volcanics from central and southern Africa**

Omar Elkhaligi



*Photo by A.D. Combe*

A thesis submitted for the degree of Master of Research



**MACQUARIE**  
University  
SYDNEY · AUSTRALIA

Faculty of Science and Engineering

Department of Earth and Planetary Sciences

Submitted: 09/01/18

Photo on title page by Arthur Delmar Combe taken from the north end of Lake Mutanda looking over the major volcanoes Muhavura, Mgahinga and Sabinyo. From: COMBE, A. D. & SIMMONS, W. C. 1933. The volcanic area of Bufumbira, Part I: The Geology of the Volcanic Area of Bufumbira, South-West Uganda, Government Printer, South Africa.

## **Abstract**

Olivines from mantle derived igneous rocks, specifically kimberlites from the Kalahari craton and alkaline to ultrapotassic mafic volcanics from the western branch of the East African Rift System from two distinct volcanic fields of Toro-Ankole and Virunga, were analysed by LA-ICP-MS to determine their minor and trace element concentrations.

Olivine trace element geochemistry has gained increasing attention over the last decade as even though olivine has a limited ability to uptake trace elements early crystallization gives it the ability to record the most primitive unaltered compositions of the melt. These minor and trace element characteristics are compared to the growing range of olivine datasets sourced from a range of tectonic environments as to ascertain clues to the composition and conditions of the mantle source of these melts.

A crustal component is inferred to be present in leucite basanites and potassic trachybasalts from the Virunga field due to the elevated Li concentrations in olivine (9.48 ppm), well above the mantle average of 3 ppm. Elevated V/Sc in one of the ugandites from Toro-Ankole is caused by a phlogopite component in the source, and not variation in oxygen fugacity.

### **Acknowledgements**

I would like to thank my supervisor Prof. Stephen Foley for the time and effort he spent assisting and advising me. Thank you to Prof. Dorrit Jacob for supplying the kimberlite sections and thank you to Rosanna Murphy and Lucy McGee for your assistance on the LA-ICP-MS. Thank you to Manal Bebbington for your assistance in polishing samples. Thank you to Robert Deutsch, Stephan Buhre and Nora Groschopf at Mainz University for the EMP analysis of my samples. Thank you to Bronwyn Campbell for assisting with proofreading and attempting to teach me how to use commas.

### **Statement of originality**

No part of this work has been previously submitted elsewhere, to any university or institution. All parts of this thesis are the original work of the author except where stated.

Signed:  \_\_\_\_\_ Date: 09/01/18

## **Contents**

1.	Introduction .....	1
1.1	Localities .....	2
1.1.1	Western branch of the East African Rift System .....	3
	Toro-Ankole .....	4
	Katwe-Kikorongo .....	5
	Bunyaraguru .....	5
	Katunga .....	6
	Virunga .....	6
	Previous olivine trace element studies from K-rich volcanism .....	7
1.1.2	Kalahari craton .....	8
	Frank Smith .....	8
	Roberts Victor .....	9
	Letlhakane .....	9
	Previous olivine trace element studies from kimberlites .....	10
2.	Methods .....	11
2.1	Petrographic analyses and photomicrographs .....	11
2.2	Laser Ablation - Inductively Coupled Plasma - Mass Spectrometry (LA-ICP-MS) .....	11
2.2.1	LA-ICP-MS Analyses .....	13
2.2.2	Corrections for overlaps .....	14
2.3	Electron Microprobe (EMP) .....	15
2.3.1	EMP Analyses .....	16
3.	Results .....	17
3.1	Standards .....	17
3.2	Petrographic description of olivines .....	17
3.3	Olivine compositions by EMP analyses .....	19
3.4	Olivine compositions by LA-ICP-MS analyses .....	22
5.	Conclusions .....	48
5.1	Western branch East African Rift System .....	49
5.2	Kalahari craton .....	50
5.3	Future directions .....	50
6.0	References .....	ix
7.0	Appendices .....	xv

## **List of figures**

**Figure 1.1:** Sample localities and simplified regional geology overlayed on political borders. Modified from Field et al., (2008), Beg et al., (2009), and Link et al., (2010).

**Figure 1.2:** Sample locations and simplified regional geology of the northern portion of the western branch of the East African Rift System, north of South Kivu. Modified from Koehn et al., (2010), Link et al., (2010), Barifaijo., (2010).

**Figure 2.1:** Simplified diagram of the LA-ICP-MS unit at Macquarie University. Modified from: [http://www.analchem.ugent.be/ams\\_onderzoek\\_solid/](http://www.analchem.ugent.be/ams_onderzoek_solid/)

**Figure 2.2:** Simplified diagram of an EMP with a WDS detection system. Modified from Goldstein et al., (2003).

**Figure 3.1:** Olivine grain typical of samples from the western branch of the East African Rift, from sample C3946 olivine surrounded by melilitite laths PPL image, laser ablation crater visible in the centre of the image.

**Figure 3.2:** Olivine grain typical of the kimberlite samples from the Kalahari craton, from sample RVK1 kimberlite, fractures filled with serpentine alteration (brown), PPL. Only a portion of the grain is imaged. Laser ablation crater visible in the centre of the image.

**Figure 3.3:** EMP analyses - SiO<sub>2</sub> vs MgO, and SiO<sub>2</sub> vs FeO. Key presented for the analyses of this study. Data coloured by location, with Virunga olivines in blue, Toro-Ankole olivines in red, and Kalahari olivines in black.

**Figure 3.4:** LA-ICP-MS analyses of first-row transition metals in addition to the post-transition metal Ga plotted against Mg#. Same key as Figure 3.3.

**Figure 3.5:** LA-ICP-MS analyses of selected elements (Li, Na, Ca, Y, Al and P) against Mg#. Same key as Figure 3.3.

**Figure 4.1:** Mg# vs Ni of olivine spot analyses. Modified from Herzberg, (2011), Sørensen et al., (2015) and Bussweiler et al. (2015). Primary peridotite derived magma field ranging in composition from 8-38 % MgO (green), and the evolution path of melts ranging in composition from 8-20 % MgO (grey), calculated by Herzberg, (2011). Key presented for the analyses of this study in addition to the relevant analyses from Foley et al., (2011). Data coloured by location with Virunga olivines in blue, Toro-Ankole olivines in red, and Kalahari olivines in black.

**Figure 4.2:** Mg# vs Fe/Mn of olivine spot analyses: Modified from Herzberg, (2011) and S ager et al., (2015).  $-(\text{Cpx}+\text{Ol})$  = fractionation path from removal of clinopyroxene and olivine,  $-\text{Ol}$  = fractionation path from the removal of olivine alone. Primary peridotite derived magma field ranging in composition from 8-38% MgO (green), and the evolution path of melts ranging in composition from 8-20% MgO (grey), calculated by Herzberg, (2011).

**Figure 4.3:** Mg# vs Ca of olivine spot analyses, Modified from Herzberg, (2011) and S ager et al., (2015). Primary peridotite derived magma field ranging in composition from 8-38% MgO (green), and the evolution path of melts ranging in composition from 8-20% MgO (grey), calculated by Herzberg, (2011).

**Figure 4.4:** Mg# vs Ni/Co of olivine spot analyses. Modified from Sobolev et al., (2007) and Foley et al., (2013). Line at Ni/Co 20 is representative of the average value from the bulk silicate Earth, core, and mantle (McDonough and Sun, 1995). Values above the line have Ni/Co ratios indicative of mantle melting with the involvement of pyroxenite and values below the line indicative of fractional crystallization (Sobolev et al., 2007).

**Figure 4.5:** Cr vs Mn of olivine spot analyses. Modified from Veter et al., (2017). Continental peridotite field (grey) defined by  $1000 \pm 300$  ppm Mn and variable Cr concentration (Veter et al., 2017). Fractionation trend illustrated by decreasing Cr and increasing Mn. Oceanic trend illustrated by a mutual increase in Mn and Cr.

**Figure 4.6:** Co, Sc, Al, and Mn vs Ni. Modified from Foley et al., (2013). Oceanic trend indicates the involvement of pyroxenite in the source as inferred from OIB data (Neumann et al., 1999, Foley et al., 2013). Orogenic trend indicates involvement of phlogopite-pyroxenite or amphibole-pyroxenite in the source as inferred from Mediterranean lamproites (Prelevi  and Foley, 2007, Foley et al., 2013).

**Figure 4.7:** Mn/Fe vs Ni/Mg. Modified from Sobolev et al., (2007) and Ammannati et al., (2016). Fields from Ammannati et al., (2016) and references therein. Low Mn/Fe and high Ni/Mg is associated with the presence of pyroxenite in the source (Sobolev et al., 2007). Extremely low Mn/Fe can be caused by the presence of phlogopite in the source (Veter et al., 2017) and high Mn/Fe from carbonate metasomatism of the source (Ammannati et al., 2016).

**Figure 4.8:** Li vs Ti. Modified from Ammannati et al., (2016). Mantle band defined by Li <3 ppm and varying Ti concentrations (Foley et al., 2013, Veter et al., 2017). Addition of

crustal component indicated by Mediterranean lamproites in the form of recycled subducted continental crustal material Prelević et al., (2013).

**Figure 4.9:** Mn vs log Al and log Zr vs Sc. Modified from De Hoog et al., (2010).

Discriminatory plots taking advantage of partition coefficients between olivine, garnet, and spinel as well as temperature and pressure effects (De Hoog et al., 2010). New key used for this plot.

**Figure 4.10:** V/Sc vs Ni. Modified from Veter et al., (2017). V/Sc can potentially be used as a proxy for the redox state of the system, with high V/Sc indicating reducing conditions and Low V/Sc indicating oxidized conditions. Peridotite field constructed from values from Kaeser et al. (2006) and De Hoog et al., (2010).

**Figure 5.1:** A summary of the western branch of the East African Rift System. TA= Toro-Ankole V= Virunga. A= potential primary kamafugitic source of the Virunga field. B = magmas derived from clinopyroxene and olivine fractionation. C= magmas derived from olivine fractionation and elevated Li from crustal contamination. D= slightly fractionated kamafugitic source that has undergone carbonate metasomatism E= unfractionated kamafugitic source F = kamafugitic source that has undergone phlogopite metasomatism or interaction.

### **List of tables**

**Table 1:** Averaged EMP olivine analyses in wt% oxide.

**Table 2:** Averaged LA-ICP-MS olivine analyses in ppm.

**Table 3:** Results of external standard and reference material analyses.

**Table 4:** EMP conditions table.

**Table 5:** Standard deviations EMP olivine analyses in wt% oxide.

**Table 6:** Standard deviations LA-ICP-MS olivine analyses in ppm.



## **1. Introduction**

---

Olivine is the first silicate mineral that crystallizes as the liquidus phase from Mg-rich, mantle derived melts, and because of this, it has the potential to serve as a carrier of information regarding the source composition and conditions of near unfractionated magmas (Foley et al., 2011, Foley et al., 2013). The Mg# ( $100 \times \text{Mg}/(\text{Mg} + \text{Fe})$ ), is the only major compositional difference in olivines, therefore is of limited use outside of its ability to identify the degree of fractionation experienced by mantle melts (Herzberg, 2011). Recently, however, olivine trace element abundances have been used to make inferences about the mineral composition of their source (Foley et al., 2011).

This field of research has gained momentum over the last decade, with early researchers (Sobolev et al., 2005, Sobolev et al., 2007, Kamenetsky et al., 2007) focusing on compatible trace elements (e.g. Ni, Cr and Mn) that were present in concentrations measurable with an Electron Microprobe (EMP) set up for high precision measurements with long counting times. Later, as Laser Ablation-Inductively Coupled Plasma-Mass Spectrometry (LA-ICP-MS) became the primary analysis technique, there was a shift to include less compatible and incompatible elements to the field of focus (De Hoog et al., 2010, Foley et al., 2011). This study aims to build upon the field of olivine trace element analysis as a petrogenic discrimination tool, by analysing mantle derived volcanics from central and southern Africa.

This study will use olivine analyses from ultra-potassic kamafugites, K-rich varieties of basanites and trachybasalts, and kimberlites.

Ultra-potassic kamafugites (katungite-mafurite and ugandite) are associated with deep melting (>140 km) in rift environments on craton edges (Foley et al., 2012), in some cases with a subduction influence (Tappe et al., 2003). K-rich varieties of basanites and alkali basalts, occur in well-developed rift environments with shallower melting (80-100km) (Rosenthal et al., 2009, Foley et al., 2012). Kimberlites mostly occur within craton environments, with source regions below cratonic lithosphere, with source depths, potentially up to 500 km (Field et al., 2008). Diamond bearing kimberlites must pass through sub-continental-lithospheric-mantle (SCLM), that is in the diamond stability zone of >130-150 km (Stachel and Harris, 2008).

## 1.1 Localities

The samples in this study originate from two distinct areas with different tectonic regimes (Figure 1.1). The samples from central Africa all come from a portion of the western branch of the active East African Rift System that is located within Uganda and Rwanda (Woolley, 2001, Link et al., 2010). The samples from southern Africa overlie the Kalahari craton and are spread across South Africa and Botswana (Field et al., 2008, Begg et al., 2009).

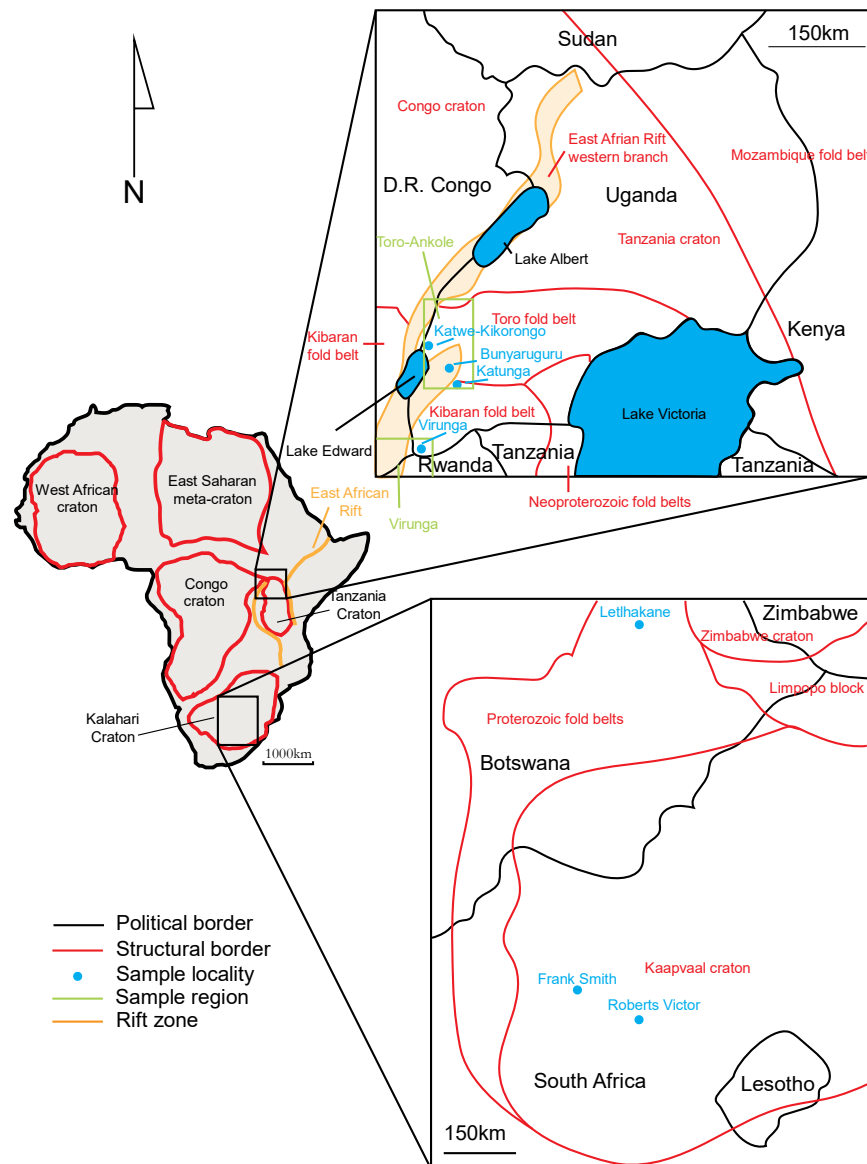


Figure 1.1: Sample localities and simplified regional geology overlaid on political borders. Modified from Field et al., (2008), Beg et al., (2009), and Link et al., (2010).

### **1.1.1 Western branch of the East African Rift System**

The western branch of the East African Rift System is home to a wide range of volcanism, ranging from tholeiites to kamaugites (Furman, 1995, Rosenthal et al., 2009, Pouclet et al., 2016). There are four main locations of Cenozoic volcanism along the rift. From south to north these are Rungwe, South Kivu, Virunga and Toro-Ankole (Ebinger, 1989, Rosenthal et al., 2009). The two northernmost sections of the western branch Cenozoic volcanism, Toro-Ankole and Virunga, are the focus of this study (Figure 1.1). The South Kivu and Rungwe fields are located off the inset map in Figure 1.1. South Kivu is further south in the western branch of the East African Rift system just south of Lake Kivu, and Rungwe is further south in the rift, just north of Lake Malawi (Rosenthal et al., 2009).

The Ugandan portion of the western branch that contains Toro-Ankole (Figure 1.2) is dominated by the Kibarian and Ubendian fold belt, along with recent rift sediments and volcanism (Figure 1.2) (Link et al., 2010). The Kibarian is represented in southwest Uganda by the Proterozoic low grade metamorphic units of Karagwe-Ankolean (Barifaijo et al., 2010, Link et al., 2010). The Ubendian (Toro) fold belt is represented by the older mica schists and amphibolites of the Buganda-Toro unit (Koehn et al., 2010, Link et al., 2010). These are underlain by the Archean to Paleoproterozoic basement, that consists of gneissic-granulite facies rocks, portions of which have been subsequently melted into migmatites and granites during Kibarian and Ubendian deformation events (Barifaijo et al., 2010, Koehn et al., 2010, Link et al., 2010).

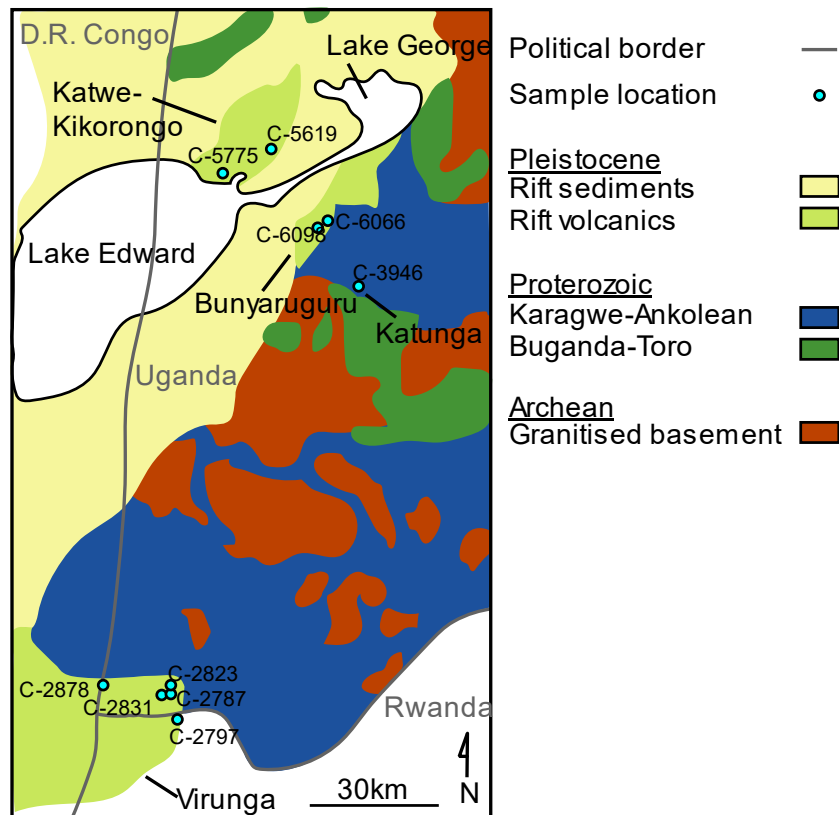


Figure 1.2: Sample locations and simplified regional geology of the northern portion of the western branch of the East African Rift System, north of South Kivu. Modified from Koehn et al., (2010), Link et al., (2010), Barifaijo., (2010).

### **Toro-Ankole**

Toro-Ankole is sometimes subdivided into two sections based upon the types of volcanism observed (Eby et al., 2003). To the north of the area lies the Fort Portal and Ndale field, which are dominated by extrusive carbonatite (Eby et al., 2009), and to the south lie the Katwe-Kikorongo and Bunyaruguru fields (Eby et al., 2003), as well as the isolated Katunga volcano (Tappe et al., 2003). This study focuses on the southern fields of Toro-Ankole, where olivines are more abundant as phenocrysts (Figure 1.2). Volcanism in the southern half of Toro-Ankole consists of a variety of potassic to ultrapotassic extrusive rocks that are silica-undersaturated (Eby et al., 2003, Tappe et al., 2003, Rosenthal et al., 2009), as well as some carbonatites (Stoppa et al., 2000).

Xenoliths in Toro-Ankole include pyroxenite, peridotite, and glimmerite at Katwe-Kikorongo (Lloyd, 1981). Bunyaruguru xenoliths consist of pyroxenite, glimmerite, wehrlite, and dunite

(Muravyeva and Senin, 2016, Muravyeva and Senin, 2018). The source of the Toro-Ankole volcanism is interpreted to have undergone metasomatism by two distinct metasomatic agents (Rosenthal et al., 2009); a phlogopite rich MARID metasomatism followed by carbonate metasomatism (Muravyeva and Senin, 2018).

### **Katwe-Kikorongo**

Samples C5775 and C5619 used in this study are from the Katwe-Kikorongo volcanic field, with C5775 being a katungite from the Katwe crater (Holmes, 1950, Tappe et al., 2003), and C5619 a leucite ankaratrite from the Mbuga crater (Holmes, 1952, Tappe et al., 2003). Previous work on these samples include whole rock major and trace element analyses of both samples by Tappe et al. (2003), in addition to whole rock, Rb/Sr, Sm/Nd and Lu/Hf, by Rosenthal et al. (2009).

The field itself is wedged between Lake Edward and the Ruwenzori horst, and comprises many small craters (Holmes, 1952). Most of the field is comprised of a variety of pyroclastic material, including juvenile, accessory and accidental ejecta (Woolley, 2001). Carbonatitic rocks have also been associated with this field (Von Knorring, 1967).

### **Bunyaraguru**

Samples C6098 and C6066 are from the Bunyaraguru volcanic field. C6098 is a ugandite from the Kyamuhogo crater (Holmes, 1945, Tappe et al., 2003), and C6066 is a mafurite from the Mafuru crater (Holmes, 1942, Tappe et al., 2003). Previous work on these samples include whole rock major and trace element analyses of both samples by Tappe et al. (2003), in addition to whole rock, Rb/Sr, Sm/Nd and Lu/Hf by Rosenthal et al. (2009), as well as Re/Os for sample C6098.

The Bunyaraguru field, which is sometimes referred to as Kichwamba, occurs to the east of Katwe-Kikorongo, with its northern edge contacting Lake George. The Bunyaraguru field is dominated by tuffs and craters, with occasional lavas (Woolley, 2001). The tuffs contain ample xenoliths, many from the basement geology, including pyroxenite, biotite pyroxenite and glimmerite (Combe and Holmes, 1945), with some of these pyroxenites showing evidence of metasomatism (Lloyd, 1981). All of the kamafugitic rocks (katungite, mafurite and ugandite) are present (Woolley, 2001).

### **Katunga**

C3946 is a katungite from the eastern foot of the isolated Katunga volcano, which lies to the southeast of the Bunyaraguru volcanic field (Tappe et al., 2003). An account of the volcano can be found in Combe (1937), and of the lava itself in Holmes (1937). Whole rock major and trace element analyses have been conducted by Tappe et al. (2003). In addition, whole rock, Rb/Sr, Sm/Nd, Lu/Hf and Re/Os analyses have been conducted on this sample by Rosenthal et al. (2009). The katungite at Katunga is the only location where this rock type occurs in the form of lava flows. Other parts of the flow have been sampled for whole rock element analyses (Holmes, 1950, Higazy, 1954, Le Bas, 1973).

### **Virunga**

Further south in the western branch (Figure 1.2) lies the Virunga volcanic field that spans the borders of Uganda, Rwanda and D.R. Congo. Bufumbira is the name given to the small north-eastern extremity of this volcanic field defined by the political borders of Uganda (Woolley, 2001). The field hosts many potassium-rich and silica-undersaturated leucite bearing volcanism, including, but not limited to, rocks from the kamafugitic series, basanties, trachybasalts, leucitites, trachyandesites and andesites (Barifaijo et al., 2010). Bufumbira is dominated by the major volcanoes Sabyinyo, Gahinga and Muhavura, however is scattered with many smaller cones and craters (Combe and Simmons, 1933) with the volcanism often following a north-northwest to south-southeast trend constrained by the basement geology (Holmes and Harwood, 1937).

Xenoliths from Virunga are primarily dunite, wehrlite and pyroxenite (Barifaijo et al., 2010). There have been arguments for (De Mulder et al., 1986) and against (Rogers et al., 1992) crustal assimilation in the Virunga field. Phlogopite has been inferred to be part of the mantle-sourced volcanism from the Mugogo volcano further south of the samples in this study, in Virunga (Condomines et al., 2015).

Four of the five Virunga samples are from Bufumbira, while one sample is from the Rwandan portion of the field. C2787 is a coarsely vesicular ugandite from the floor of the Katarara crater, which is located between Nyakimanga and Nyakabingo (Holmes and Harwood, 1937). C2823 is a leucite basanite from the Busalu cone, which is located between Busamba and Muganza (Holmes and Harwood, 1937). C2831 is a potassic trachybasalt from the northern foot of Muhavura, 1.2 km north-northwest of Nyarubebsa (Holmes and Harwood, 1937).

C2797 is a leucite basanite from the eastern edge of the Muhavura lava field (Simmons, 1930). C2797 is the only Virunga sample of this study located in Rwanda, from near the western shore of Lake Bulera, ~1.5 km north-northeast of Mweru (Holmes and Harwood, 1937). C2878 is a potassic trachybasalt from Gahinga, located 2 km north-northwest from the Bunagana trigonometrical station (Holmes and Harwood, 1937), approximately on the border between D.R. Congo and Uganda. To the knowledge of this author, there has been no work done on these exact samples since the work of Simmons (1930), and Holmes and Harwood (1937).

### **Previous olivine trace element studies from K-rich volcanism**

The work of this study directly builds upon that of Foley et al. (2011) and presents a significant extension to the dataset presented in their study. Their study selected three ugandites C4035, C6095 and C6099, and a leucite basanite C2896, for olivine trace element analysis, with the focus of the study being to test the accuracy of analyses by ablating cylindrical craters *versus* shallow trenches in the olivines of two samples C4036 and C2896. The ugandite C4035 is from Kakunyu crater at Bunyaraguru (Tappe et al., 2003), and the leucite basanite C2896 is from the Kako flows in the D.R. Congo (Holmes and Harwood, 1937). These two samples are integrated into the discussion of this study for comparison with other datasets, as they are from the same sampling areas and have undergone the same analytical techniques.

Other recent works that focus on olivine trace elements in potassic and ultrapotassic rocks include eastern Mediterranean lamproites (Prelević et al., 2013), Canadian allikites (Veter et al., 2017), Italian lamproites and leucitites (Ammannati et al., 2016), and Chinese shoshonites (Zhang et al., 2016).

### **1.1.2 Kalahari craton**

The Kalahari craton is a composite craton made up of the large Kaapvaal and smaller Zimbabwe craton, separated by the Limpopo microcontinent (Begg et al., 2009). To the west, these Archean cratons are surrounded by Proterozoic fold belts (Griffin et al., 2003). The Zimbabwe craton is made of two main terranes - the Tokewe terrane to the east and a younger accretionary terrane to the west (Kusky, 1998). The Kaapvaal craton is made of multiple smaller terranes, with the eastern terrane group consisting of the south-eastern terrane, a central terrane and the Pietersburg terrane (Griffin et al., 2003). The amalgamated eastern terrane collided with the western terrane at the end of the Archean (Griffin et al., 2003). The Frank Smith and Roberts Victor kimberlites lie within the western terrane of the Kaapvaal craton (Field et al., 2008).

Of the fold belts that surround the Kaapvaal and Zimbabwe craton, the Makondi fold belt is of the most interest as this is where the Letlhakane kimberlite is situated (Field et al., 2008). The Makondi fold belt is part of the Proterozoic Kheis–Okwa–Makondi belt, and is comprised of metasediments and metavolcanics that are interpreted to have formed on the passive margins of the Zimbabwe craton (Griffin et al., 2003).

### **Frank Smith**

The Frank Smith mine is a Group I kimberlite (Field et al., 2008), located south of Diamantmyn, and approximately 60 km north-northwest of the Kimberly mine. The kimberlite consists of two diatremes, the main Frank Smith diatreme and the subordinate Weltevreden pipe (Field et al., 2008). The two diatremes are connected by a dyke that is also kimberlitic in composition (Meyer et al., 1979, Field et al., 2008). Two samples studied here, FS1 and FS4, come from the Frank Smith mine.

This mine is known for pyroxene megacrysts (Meyer et al., 1979, Clarke and Pe-Piper, 1983), pyroxene-ilmenite xenoliths (Frick, 1973, Rawlinson and Dawson, 1979), sulphide nodules (Clarke et al., 1977), ilmenite nodules (Boyd and Pasteris, 1978), and peridotite xenoliths (Exley, 1982, Woodland and Koch, 2003).



### **Roberts Victor**

The Roberts Victor mine is a Group II kimberlite, primarily represented by two pipes, located 40km east of Boshof (Field et al., 2008). The emplacement age Given in Field et al. (2008) of  $127\pm 3$  Ma, is likely incorrect as the mica used for the Rb-Sr dating was from an eclogite xenolith not the groundmass of the (Allsopp and Barrett, 1975).

Roberts Victor contains a range of Archean xenoliths, dominated by eclogites, which have been the primary focus of research at the mine for several decades (Manton and Tatsumoto, 1971, Allsopp and Barrett, 1975, Windom and Boettcher, 1980, Deines et al., 1987, Jacob and Foley, 1999, Jacob, 2004, Huang et al., 2012, Kiseeva et al., 2017). Some research has been done on the subordinate peridotites xenoliths from the mine (Allsopp et al., 1968, Deines et al., 1987). While most of the xenoliths are eclogites, diamond inclusions at the mine are primarily peridotitic in composition (Gurney et al., 1984).

### **Letlhakane**

The Letlhakane mine is a Group I kimberlite (Field et al., 2008) located 10km southeast of the town of Letlhakane in Botswana. The Letlhakane mine consists of two diamondiferous pipes (Stiefenhofer, 1994). The nearby Orapa mine has been approximately dated to 93.1 Ma (Davis, 1977), which appears to be where the date of Letlhakane mine was estimated (McClenaghan, 1989), though it is unlikely that this is the true age, as the pipes are not genetically related (Field et al., 2008)

Although Letlhakane is only 40 km from Orapa, they carry different suites of xenoliths and diamond inclusions, with Letlhakane having a peridotitic character and Orapa having an eclogitic character (Deines and Harris, 2004, Stachel et al., 2004). As such, applying a similar age to the Letlhakane pipe from the Orapa pipe may be inappropriate.

Letlhakane, along with the large Botswanan diamond mines Orapa and Damtshaa, lies within the Proterozoic Makondi fold belt (Field et al., 2008), which is unusual for a diamond bearing kimberlite (O'Neill and Moresi, 2003). It is thought that the fold belt overlies the Archean Zimbabwe craton (Stiefenhofer et al., 1997, Borst, 2012), as the underlying mantle is 150 km thick and has a cratonic geotherm (Field et al., 2008).

### **Previous olivine trace element studies from kimberlites**

Kimberlites are a type of volcanism distinct from the K-rich volcanism in the western branch of the East African Rift, though both are thought to be derived from partial melting of metasomatically altered mantle (Mitchell, 1986, Foley et al., 1987). Recent studies have attempted to determine the phenocrystic or xenocrystic origin of olivine in kimberlites (Brett et al., 2009, Bussweiler et al., 2015). These have added to the argument that morphological features of macrocryst and groundmass olivines in kimberlites are not distinguishing features for phenocrysts or xenocrysts in their own right (Bussweiler et al., 2015).

This study aims to reveal compositional inhomogeneities and/or depth variation in the source(s) of these low volume exotic volcanics.

## **2. Methods**

---

A total of 14 pre-prepared 30 µm thick polished thin sections were chosen for geochemical analyses. From the western branch of the East African Rift System, ten samples were selected, with most sourced from the Holmes collection at the University of Durham/Cambridge and provided by Professor Stephen Foley. From the Kalahari craton, four kimberlite samples were selected, provided by Professor Dorrit Jacob.

### **2.1 Petrographic analyses and photomicrographs**

Clean spots on olivines were chosen both under plane polarised light (PPL) and reflected light (RL) as to find the cleanest grains possible free from surface and penetrating cracks or inclusions. Sites were chosen to allow a large spot size (up to 150 µm). Ten spots were chosen per slide (one slide only had eight points due to limited suitable sites) so as to allow for a good spread of data. However, there was not much freedom in site selection due the ubiquity of cracks and inclusions. Enough space was allowed for electron microprobe (EMP) spot at least 10 µm away from the laser ablation hole to minimise interference and obtain accurate elemental quantification. In ideal circumstances samples would have been EMP analysed before LA-ICP-MS in the exact spot of analysis instead of next to it, however an EMP was not immediately available at the time of analysis. Conducting the EMP analyses afterwards has the advantage of knowing exactly where the laser ablation crater location is.

### **2.2 Laser Ablation - Inductively Coupled Plasma - Mass Spectrometry (LA-ICP-MS)**

LA-ICP-MS involves the coupling of a laser ablation sample introduction system to an ICP-MS mass to charge analysis system (Sylvester, 2008), a typical layout shown in Figure 2.1 with the values of parameters used in this study integrated into the graphic. Laser ablation is achieved by using pulsed laser. In the case of this study an excited dimer “excimer” laser was used, the wavelength being dependant on the molecule pair used. Excimer lasers offer the advantage of having greater focusability over solid state lasers (Stafe et al., 2010). The

ablation of the solid occurs in a sealed container so that the ejected material can be carried to the ICP-MS unit via a carrier gas such as helium in the form of an aerosol (Sylvester, 2008).

The ICP is generated via the use of a radio frequency (RF) alternating current signal in a coil surrounding an argon gas flow, which in turn induces an RF magnetic field. With the aid of an initial high voltage spark to ionise a few argon atoms a chain reaction follows which results in the argon gas inside the coil forming a positively charged plasma with temperatures between 6000-1000 K. As the ablated material is carried through this plasma it is first atomised then ionised forming mostly positive ions as the argon plasma strips electrons from the sample. The ionised material then enters the mass spectrometer unit, initially being filtered by a sampler cone then skimmer as the sample transitions from an atmospheric pressure environment to that of a vacuum. Carried through the unit by a strong negative voltage at the far end of the mass spectrometer, the ionised atoms of the sample first pass through focusing optics which narrow and focus the beam of ions and at the same time get rid of unwanted uncharged species, such as unionised sample or photons (in the Agilent 7700cx the unwanted species are removed at the sampler cone stage of the apparatus).

This focused ion beam then enters the mass separation device, which in this case is a quadrupole mass analyser. In this mass analyser, the ions are filtered by a pair of rods with direct current and a pair of rods with alternating current that when combined act as a low pass and a high pass filter simultaneously only allowing one target mass/charge unit through at a time with all other mass/charge units being neutralised as they collide with the rods. The target ion then passes through to the detector, which in this case is a discrete dynode detector operating as an electron multiplier amplifying the signal generated by the ion. The mass analyser sequentially selects different mass/charge ratios at a rapid rate to the point it is considered to be a pseudo-simultaneous acquisition (Thomas, 2013).

This signal, which is either a count per a second (CPS) value or an analogue voltage converted to CPS equivalent is then analysed by a software package which converts these values to a semi-quantitative value, with a known value from external calibration this can be converted to a quantitative result. These data can then be viewed in a processing package such as GLITTER which provides an interface in order to filter, correct and select data along with a database of standards along with the ability to export the data into .csv files (Griffin et al., 2008, Sylvester, 2008).

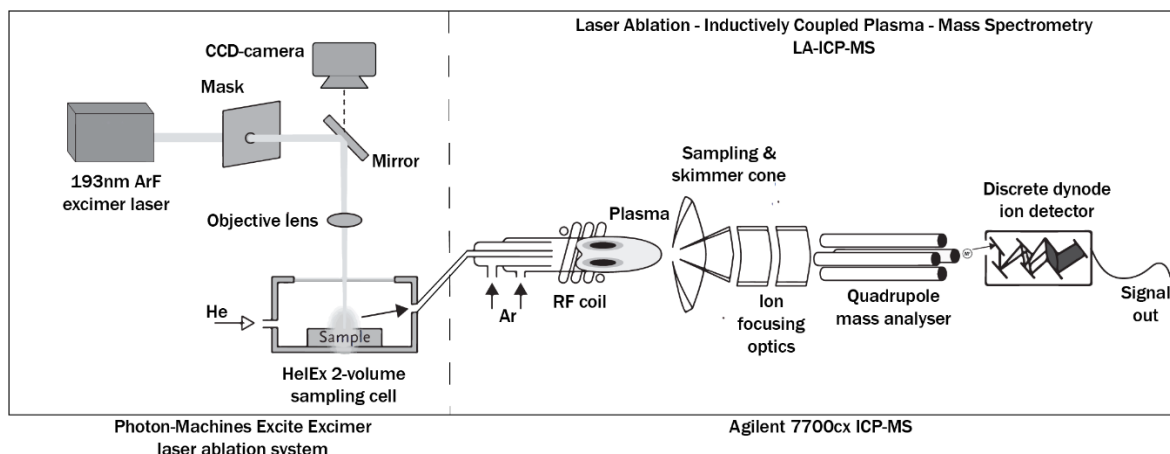


Figure 2.1: Simplified diagram of the LA-ICP-MS unit at Macquarie University. Modified from: [http://www.analchem.ugent.be/ams\\_onderzoek\\_solid/](http://www.analchem.ugent.be/ams_onderzoek_solid/)

### **2.2.1 LA-ICP-MS Analyses**

Samples were analysed for trace elements by LA-ICP-MS at the Geochemical Analysis Unit in Macquarie University, Sydney, Australia.

Thin sections were run alongside National Institute of Standards and Technology (NIST) 610 and 612 glasses as External Standards (Jochum et al., 2011), a United States Geological Survey reference material BCR-2G (Jochum et al., 2009) as a reference standard and two unofficial San Carlos Olivines (SCO) as internal standards (Fournelle, 2011). The standards were run at the beginning and end of each thin section, along with being used in the ICP-MS initial calibration. EMP analyses on each of the target spots was conducted to act as an internal standard for the quantification of the ICP-MS data. Analyses were conducted over three separate days.

Target masses were analysed on an Agilent 7700cx series ICP-MS with an argon carrier and plasma gas using MassHunter interface software. This was coupled to a Photon-Machines Excite Excimer laser ablation system which used a 193 nm ArF excimer laser in conjunction with a two volume HelEx sample chamber using with helium as a purge gas with CHROMIUM interface software. 85  $\mu\text{m}$  spot sizes were used for standards and 85-150  $\mu\text{m}$  spot sizes were used for unknown olivine grains. Large spot sizes were chosen to ablate as much material as possible while avoiding cracks and leaving enough space for EMP analysis. Large spot sizes were chosen as the thin sections were quite thin (<30  $\mu\text{m}$ ) compared to normal LA-ICP-MS

thick sections (100-200  $\mu\text{m}$ ). A large spot size is advantageous as it avoids loss of material to the crater wall and maximises ablated sample volume (Foley et al., 2011). 29 seconds of background and 59 seconds of ablated sample were collected. 295 laser shots at a rate of 5 Hz were ablated at the chosen site with a laser flux of 5  $\text{J}/\text{cm}^2$  with a 20 second delay between samples to allow the line to clear.  $^{43}\text{Ca}$  was chosen as the isotope for the standards and reference material while  $^{29}\text{Si}$  was chosen for the samples to avoid potential interference. For most elements a detection limit better than 3 % and analytical precision better than 6 % was achieved. An exception being, Y that typically had an analytical precision better than 10 %. Ba, Sr, Zr and the Lanthanoids frequently had analytical precision worse than 20 % up to 80 % in some cases many more values being below the minimum detection limit entirely. Data were processed with GLITTER software (Griffin et al., 2008) for real time analyses of data quality including monitoring for cracks and inclusions.

### **2.2.2 Corrections for overlaps**

Potential interferences in ICP-MS are induced by the method of detection being mass on charge ( $m/z$ ), that is not always a property unique to each isotope (Thomas, 2013).

There are three main sources of overlap (Thomas, 2013). The first is direct overlap of an isotope of one element with the isotope of another e.g.  $^{40}\text{K}$  on  $^{40}\text{Ca}$ . The second being doubly charged species e.g.  $^{24}\text{Mg}^{2+}$  on  $^{12}\text{C}^+$  and the third being overlap of polyatomic species which are most commonly argides, oxides and hydroxides, though hydroxides are significantly reduced in LA-ICP-MS as compared to traditional solution ICP-MS which uses water as a solute carrier (Gilbert et al., 2017, Thomas, 2013).

There are several ways of eliminating or accounting for this overlap. For direct overlap careful selection of target isotopes can eliminate the majority of cases. Background subtraction accounts for a variety of overlaps caused by the carrier gasses and is automatically handled in GLITTER software. This background subtraction does not account for species introduced only upon ablation which for olivine are Si, Mg, Fe and O as well as their interactions with the Ar carrier gas. Polyatomic overlaps can be accounted for via subtraction of the discrepancy from a known standard value (De Hoog et al., 2010), though matrix matching is essential (Gilbert et al., 2017) and a suitable standard was not available. The second way to overcome polyatomic interference is to select isotopes that are interference free (De Hoog et al., 2010),

which for this study included  $^{25}\text{Mg}^{40}\text{Ar}^+$  on  $^{65}\text{Cu}^+$  and  $^{26}\text{Mg}^{40}\text{Ar}^+$  on  $^{66}\text{Zn}^+$  both overcome by selecting relatively interference free isotopes  $^{63}\text{Cu}^+$  and  $^{67}\text{Zn}^+$  respectively.

The third way of accounting for polyatomic overlap is to measure multiple isotopes, with known interferences, and perform a calculated correction (De Hoog et al., 2010, Foley et al., 2011). This calculation must be done for the monoisotopic  $^{45}\text{Sc}$ . Measuring  $^{44}\text{Ca}$  and  $^{43}\text{Ca}$ , the amount of  $^{28}\text{Si}^{16}\text{O}$  could be established from the discrepancy between the two values and their natural abundance ratios (De Hoog et al., 2010, Foley et al., 2011). With the assumption of uniform reaction of Si isotopes with  $^{16}\text{O}$ ,  $^{29}\text{Si}^{16}\text{O}$  could be determined from natural abundances, and subtracted from the  $^{45}\text{Sc}$  value, (De Hoog et al., 2010, Foley et al., 2011). Sc corrections ranged from ~3-9 %.

NIST 612 was used as the machine standard to correct for internal drift and oxide production through Th/ThO ratio, which is automatically handled by GLITTER software. The one exception being  $^{63}\text{Cu}$ , for which BCR-2G was used as the machine standard, to avoid  $^{23}\text{Na}^{40}\text{Ar}$  interference, a potential issue for the standardisation to NIST 612 as it contains 14 wt%  $\text{Na}_2\text{O}$  (Foley et al., 2011). Atomic weight values were sourced from Meija et al., (2013a) and isotope abundances from Meija et al., (2013b).

### **2.3 Electron Microprobe (EMP)**

An EMP takes advantage of characteristic x-rays generated by the interaction of a focused electron beam with the orbital electrons of atoms within a sample. There are two ways of measuring these x-rays with one being Energy-Dispersive X-ray Spectroscopy (EDS) and the other Wavelength Dispersive X-ray Spectroscopy (WDS) with an EMP taking advantage of the latter for better resolution (Figure 2.2), however EMP are also often fitted with additional EDS detectors (Goldstein et al., 2003, Reed, 2005).

This method is possible as energy is proportional to wavelength  $E = \frac{hc}{\lambda}$ . This allows precise photon energy measurements to be conducted by isolating specific wavelengths by taking advantage of Bragg's Law  $n\lambda = 2d \sin\theta$  in conjunction with a specific analysing crystal and orientation. The disadvantage of WDS is that it can only measure one wavelength at a time (per a detector) which slows down the process while EDS can measure all energies near simultaneously at the cost of resolution and sensitivity (Goldstein et al., 2003).

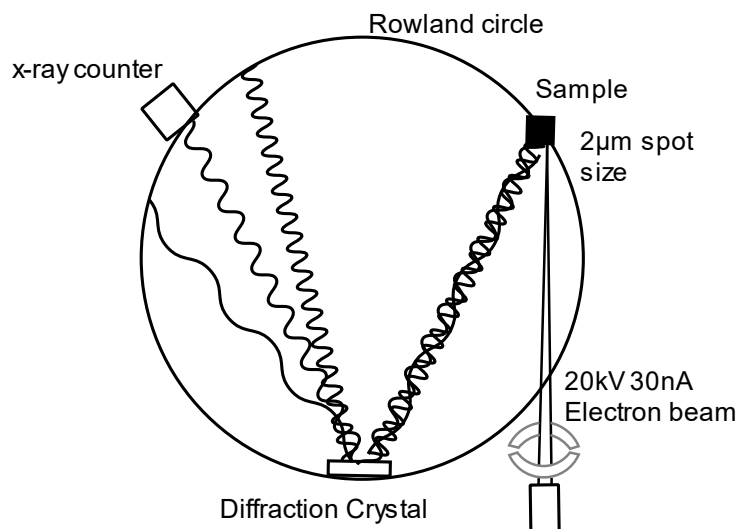


*Figure 2.2: Simplified diagram of a EMP with a WDS detection system. Modified from Goldstein et al., (2003).*

### **2.3.1 EMP Analyses**

Prior to EMP analyses slides were polished with diamond paste as to remove the ejecta that was caused by the laser ablation in the LA-ICP-MS analyses. Olivines were analysed for major and minor elements by WDS EMP, at the Institute of Geosciences in Johannes Gutenberg University Mainz, on a Jeol JXA 8200, on the 27<sup>th</sup> of July 2017. An acceleration voltage of 20 kV, a current of 30 nA and a beam diameter of 2 µm was used for spot analysis. Peak counting times, external standards, overlaps and additional information are detailed in the appendix (Table 3). A San Carlos olivine was used as an internal replicability standard. Oxide ZAF corrections (Reed, 1965, Scott and Love, 1992), were applied by the operator using the integrated software.



### **3. Results**

---

Results are presented as a series of tables, which contain the averaged concentration of all olivine grains in individual samples. Also included are a selected series of plots presenting the results of the individual spot analyses.

The individual samples are grouped by tectonic location, as discussed in the introduction.

#### **3.1 Standards**

The replicability of the NIST610 standard and the BCR-2G reference material used in this study's LA-ICP-MS analyses are presented in the appendix (Table 4). Most averaged values for NIST610 fall within GeoReM error (Jochum et al., 2009, Jochum et al., 2011), apart from Ba, Sr, Cr, V and B, which fall within GeoReM values when the 2SD error of analyses over the course of this study is taken into consideration. Ti and B returned the values furthest from GeoReM values, but still possess overlapping error values when both the 2SD error of this study and the 2SD error of GeoReM are taken into consideration.

For BCR-2G, again most averaged values fall within GeoReM error, apart from Al, P, Ba, La, and Yb, which all still possess overlapping error values when both the 2SD error of this study and the 2SD error of GeoReM are taken into consideration. However, B, Zn, Ga, Ce and Gd fall outside GeoReM values even when errors are taken into consideration. B was the only element to have poor replicability for both standards.

#### **3.2 Petrographic description of olivines**

Olivines from the western branch of the East African Rift are primarily euhedral to subhedral. An exception to this is C5775, which has a single large (~5 mm) anhedral grain, which is, however chemically similar to the rest of the grains of the sample, and C5619, which has several grains that appear anhedral due to alteration. Most olivine grains have little to no reaction rims, with the exception of C5775 and C5619. Olivine grain sizes ranged from <0.1 to ~5 mm, with most sampled olivines being 0.75 to 2 mm, and the smallest being ~0.3 mm. Moderate fracturing is common in almost all olivines, though some of the smaller olivines (<0.45 mm) were without fractures. Fractures viewed in thin sections contained no major visible alteration or replacement. An olivine grain typical of the western branch samples is pictured in (Figure 3.1).

Olivines from the kimberlites of the Kalahari craton are consistently anhedral in shape. Grains ranged in size between ~0.15 mm and 15 mm, and were very poorly sorted. All olivines were heavily fractured, with considerable alteration along fractures viewed in thin section. Many smaller grains have been completely replaced by alteration products such as serpentine, leaving only pseudomorphs of olivine. No Kalahari olivines measured were smaller than 3 mm, due to the need to avoid fracturing and alteration. An olivine grain typical of the Kalahari samples is pictured in (Figure 3.2).

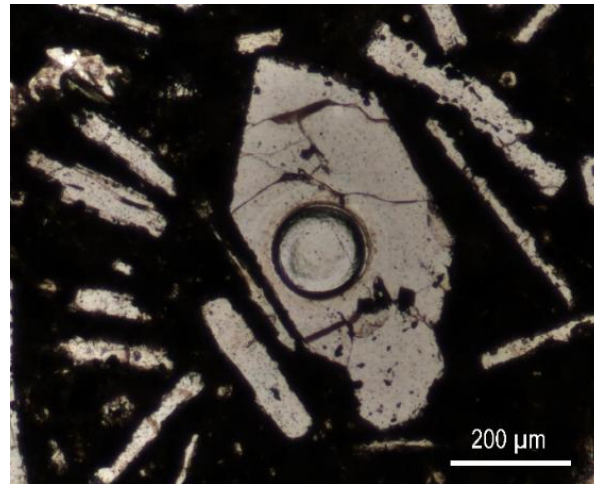


*Figure 3.1: Olivine grain typical of samples from the western branch of the East African Rift, from sample C3946 olivine surrounded by melilitite laths PPL image, Laser ablation crater visible in the centre of the image.*



*Figure 3.2: Olivine grain typical of the kimberlite samples from the Kalahari craton, from sample RVK1 kimberlite, fractures filled with serpentine alteration (brown), PPL. Only a portion of the grain is imaged. Laser ablation crater visible in the centre of the image.*

### **3.3 Olivine compositions by EMP analyses**

#### **Major elements**

Major and minor element data from EMP analyses of the Virunga, Toro-Ankole and Kalahari olivine populations are outlined in the following section and summarised in (Table 1).

Standard deviations are available in the appendix (Table 5). The focus of the EMP data are the major element oxides MgO, SiO<sub>2</sub>, FeO and the calculated Mg# ( $100 \cdot \text{Mg}/(\text{Mg}/\text{Fe})$ ).

Individual spot analyses results for SiO<sub>2</sub> vs MgO and FeO are plotted in Figure 3.3.

Concentrations and ratios reported in the following section are averaged data from spot analyses of olivines from individual thin sections, which are then grouped by their associated field locations (Table 1).

#### **Western branch of the East African Rift**

The Toro-Ankole olivines (C5619, C5775, C3946, C6066, C6098) have a relatively narrow range of MgO concentrations. C5775 has the lowest concentration, at 45.6 wt% MgO, while C6066 has the highest concentration, 49.7 wt% MgO. The Virunga olivines (C-2831, C-2878, C-2797, C-2823, C-2787) have a wider range of MgO concentrations than those from Toro-Ankole, though a cluster of lower MgO concentrations occurs (Figure 3.3), with C2831 at 34.2 wt% MgO, C2797 at 34.5 wt% MgO and C2878 at 35.4 wt% MgO. C2823, from Virunga, has a higher concentration than the lower MgO cluster, at 41.6 wt% MgO, while C2787 has the highest concentration of the Virunga population, at 48.3 wt% MgO, placing it within the range of the Toro-Ankole olivines.

FeO concentrations have an opposite trend to MgO, with the Virunga olivines having higher concentrations than Toro-Ankole. A cluster of high FeO concentrations is present in the Virunga olivines (Figure 3.3; C2831, C2797 and C2878), with concentrations ranging between 27.2 and 28.4 wt% FeO. Of the Virunga olivines, C2823 has a relatively low FeO concentration, at 19.7 wt%. The lowest FeO concentration from Virunga is C2787, at 10.0 wt% FeO. Toro-Ankole olivines are lower in FeO than the Virunga olivines, with a narrower range. C6066 has the lowest concentration from the Toro-Ankole olivines, at 8.6 wt% FeO, while the highest concentration is seen in C5619, at 13.6 wt% FeO.

As expected, SiO<sub>2</sub> has less variation than MgO and FeO, due to SiO<sub>2</sub> being a structural element of olivine (Deer et al., 1992). The Toro-Ankole olivines have less than 1.00 wt%

variation, ranging between 40.2 wt% SiO<sub>2</sub> in C5775, and 41.0 wt% SiO<sub>2</sub> in C6066. The Virunga olivines have less SiO<sub>2</sub> than the Toro-Ankole olivines. Virunga olivine concentrations cluster, just as by FeO and MgO concentrations, with C2797 at 37.9 wt% SiO<sub>2</sub>, C2831 at 38.1 wt% SiO<sub>2</sub> and C2878 at 38.2 wt% SiO<sub>2</sub>. C2823 and C2787 from Virunga have higher concentrations, at 39.2 and 40.9 wt% SiO<sub>2</sub> respectively.

A low Mg# cluster is present in the Virunga samples (Figure 3.3), with olivines from C2797 at a Mg# of 68.4, C2831 at a Mg# of 68.0, and C2878 at a Mg# of 69.8, while C2823 is at a Mg# of 79.0, and C2787 at a relatively high Mg# of 89.5. Mg# ratios from the Toro-Ankole olivines ranges between 85.8 in C5619, and 91.2 in C6066.

### Kalahari

The Kalahari kimberlite olivines have relatively high MgO concentrations (Figure 3.3), with RVK1 having the highest of this study, at 50.6 wt% MgO, though also with LK1 having the lowest of this study, at 48.6 wt% MgO. Overall, the Kalahari olivines have the lowest FeO concentrations of this study, ranging from RVK1 at 7.41 wt% FeO, up to LK1 at 10.1 wt% FeO. The Kalahari olivines have a relatively narrow range of SiO<sub>2</sub> concentrations, between FS1 at 41.1 wt% SiO<sub>2</sub>, and RVK1 at 41.4 wt% SiO<sub>2</sub>. All Kalahari olivines have relatively high Mg#, ranging between 89.6 in LK1, and 92.4 in RVK1.

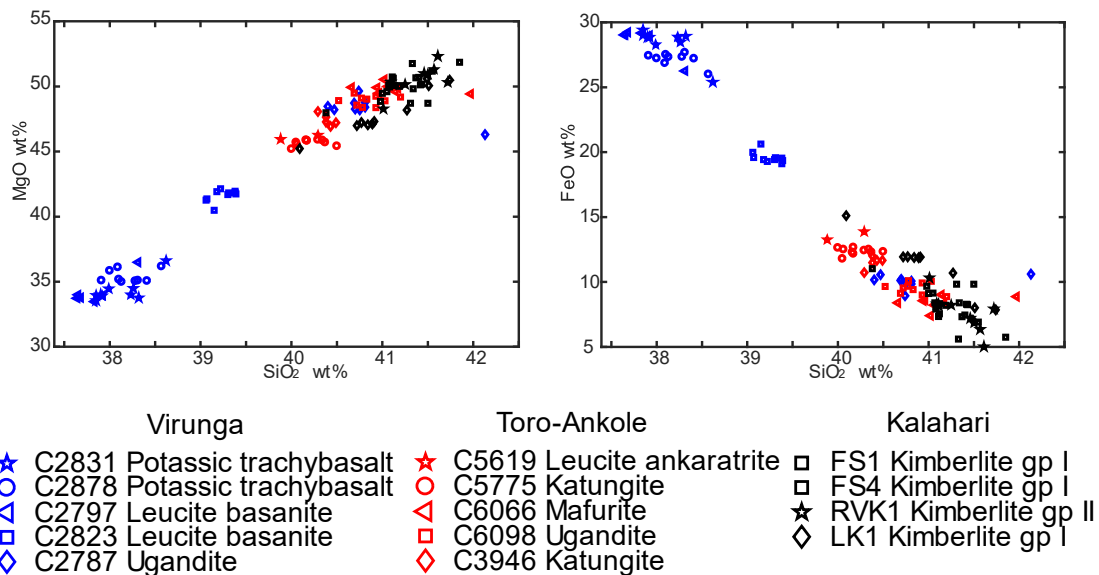


*Figure 3.3: EMP analyses - SiO<sub>2</sub> vs MgO, and SiO<sub>2</sub> vs FeO. Key presented for the analyses of this study. Data coloured by location with Virunga olivines in blue, Toro-Ankole olivines in red, and Kalahari olivines in black.*

Table 1: Averaged EMP olivine analyses in wt% oxide.

	Virunga					Toro-Ankole					Kalahari			
	C-2831	C2878	C-2797	C-2823	C-2787	C5619	C5775	C6066	C6098	C3946	FS1	FS4	RVK1	LK1
Al <sub>2</sub> O <sub>3</sub>	0.0279	0.0288	0.0262	0.0302	0.0534	0.0261	0.0146	0.0210	0.0348	0.019	0.00953	0.0114	0.00312	0.0254
SiO <sub>2</sub>	38.1	38.2	37.9	39.2	40.9	40.1	40.2	41.0	40.8	40.4	41.1	41.2	41.4	41.2
CaO	0.334	0.348	0.38	0.268	0.375	0.288	0.301	0.125	0.122	0.339	0.0408	0.0464	0.0189	0.0472
MnO	0.484	0.447	0.494	0.33	0.17	0.219	0.212	0.123	0.121	0.219	0.115	0.113	0.104	0.120
CoO	0.0277	0.0286	0.0298	0.0267	0.0262	0.0294	0.0299	0.0282	0.0275	0.0259	0.0298	0.0291	0.0302	0.0265
MgO	34.2	35.4	34.5	41.6	48.3	46.1	45.6	49.7	48.9	47.4	50.0	49.7	50.6	48.6
TiO <sub>2</sub>	0.0341	0.036	0.0436	0.0393	0.00904	0.0259	0.0318	0.0286	0.0446	0.0301	0.0264	0.0341	0.00844	0.017
Cr <sub>2</sub> O <sub>3</sub>	0.0310	0.0307	0.0225	0.0264	0.0935	0.0547	0.0412	0.113	0.0905	0.0658	0.0536	0.0498	0.0383	0.0509
FeO	28.6	27.2	28.4	19.7	10.0	13.6	12.4	8.60	9.53	11.5	8.29	8.56	7.41	10.1
NiO	0.0416	0.0434	0.0226	0.0266	0.232	0.163	0.14	0.403	0.402	0.234	0.377	0.379	0.352	0.33
V <sub>2</sub> O <sub>3</sub>	0.00344	0.00698	0.00291	0.00939	0.00336	0.0054	0.00474	0.00161	0.00891	0.00982	0.00394	0.00163	0.00324	0.00612
Total	102	102	102	101	100	101	99.0	100	100	100	100	100	100	101
Mg#	68.0	69.8	68.4	79.0	89.5	85.8	86.8	91.2	90.1	88.0	91.5	91.2	92.4	89.6

### **3.4 Olivine compositions by LA-ICP-MS analyses**

#### **Trace and minor elements**

Trace element data from LA-ICP-MS analyses of the Virunga, Toro-Ankole and Kalahari olivine populations are outlined in the following section and summarised in Table 2. Standard deviations are available in the appendix (Table 6). LA-ICP-MS analyses were used for all elements of this study except for Si, Fe and Mg. Individual spot analysis results for first-row transition metals, in addition to the post transition metal Ga, are plotted in Figure 3.4 against Mg#. Individual spot analysis results for selected elements are plotted against Mg# in Figure 3.5.

Concentrations and ratios reported in the following section are averaged data from spot analyses of olivines from individual thin section samples, which are then grouped by their associated field locations (Table 2).

#### **Western branch of the East African Rift**

Zn and Mn concentrations have strong negative correlations with Mg# for data from both the Virunga and Toro-Ankole fields, with correlation coefficients ( $r$ ) less than -0.70.

Mn concentrations have similar clustering to that of Mg# (Figure 3.4). C2797, from Virunga, has the highest average Mn concentration, at 4310 ppm, while C2831 has a concentration of 4230 ppm and C2878 of 3860 ppm. C2823 has substantially lower Mn concentrations relative to the other Virunga olivines, at 2980 ppm, with C2787 being lower again, at 1640 ppm. Mn concentrations in Toro-Ankole olivines form two clusters (Figure 3.4). C6066 and C6098 cluster at 1160 and 1140 ppm Mn respectively, while C5619, C3946, and C5775 cluster between 1890 and 2090 ppm Mn.

Zn concentrations have similar clustering to Mg# for the Virunga olivines (Figure 3.4). C2878, C2797 and C2831 from Virunga have high Zn concentrations ranging between 236 and 265 ppm. C2823 from Virunga has a Zn concentration of 167 ppm, and C2787 from Virunga has a Zn concentration of 70.1 ppm. However, the Zn populations do not appear split as they are for Mn in the Toro-Ankole olivines (Figure 3.4), with all olivines ranging between 76.4 and 99.8 ppm Zn.

Ni has a strong positive correlation with Mg# for the Toro-Ankole olivines ( $r = 0.93$ ). Similarly, Ni in the Virunga olivines appears to have a strong positive correlation with Mg# ( $r = 0.81$ ), however when C2787 (Mg# 89.5) is excluded this is reduced ( $r = -0.50$ ) (Figure 3.4). Ni concentrations have little variance in the Virunga olivines if C2787 is considered separate, with most concentrations ranging between 210 and 392 ppm. However, C2787 has a higher concentration than most of the Virunga field, with a Ni concentration of 2000 ppm. The Toro-Ankole olivines plot as two clusters of Ni concentrations (Figure 3.4), with C6066 and C6098 having 3550 and 3460 ppm Ni respectively, and C5619, C3946, and C5775 having between 1360 and 1860 ppm Ni.

Co in Virunga olivines appears to have a strong negative correlation with Mg# ( $r = -0.88$ ) that is reduced ( $r = -0.48$ ) when C2787 is excluded. Most Virunga concentrations range between 210 and 230 ppm. However, C2787 has lower concentrations than most of the Virunga field, at 174 ppm Co. Toro-Ankole Co concentrations are lower than the Virunga field, ranging between 162 and 197 ppm.

Cr has a strong positive correlation with Mg# ( $r > 0.78$ ) in both the Toro-Ankole and Virunga olivines, even when C2787 is excluded. Toro-Ankole olivines span concentrations of 137 to 703 ppm Cr. The Virunga Cr concentrations plot in two clusters, in a similar pattern to Ni concentrations (Figure 3.4). Most Virunga olivines have relatively low Cr concentrations compared to Toro-Ankole, ranging between 12.2 and 45.0 ppm, whereas C2878 has 543 ppm Cr.

Virunga has a relatively narrow range of Sc concentrations, with most olivines ranging between 5.92 and 6.71 ppm. Most variation of Sc in the Toro-Ankole olivines is due to olivine C5775 (Figure 3.4), at 7.11 ppm Sc, with the remaining olivines having concentrations between 5.19 and 4.49 ppm Sc.

V is higher in three Virunga olivines (Figure 3.4), with C2831, C2878 and C2797 having 17.0, 18.0 and 14.0 ppm V respectively. The C2823, C2787 from Virunga and Toro-Ankole olivines have less than 7.55 ppm V.

Cu concentrations are higher in the Toro-Ankole olivines than the Virunga olivines (Figure 3.4). Most Virunga olivines have less than 1.11 ppm Cu, except for C2787, which has a higher Cu concentration of 2.22 ppm. Toro-Ankole Cu concentrations are higher than Virunga, and range between 3.28 and 7.28 ppm.

Ga has a relatively narrow range of concentrations in the Virunga olivines, between 0.141 and 0.213 ppm. Toro-Ankole concentrations have a relatively wide Cu range, between 0.0928 and 0.238 ppm Ga.

For the second-row transition metal, Y, Virunga olivines form 3 clusters, with C2878, C2797 and C2831 ranging between 0.341 and 0.366 ppm, while C2823 lies at 0.111 ppm and C2787 at 0.0454 ppm. The Virunga olivines have a strong negative correlation ( $r = -0.95$ ) with Mg#. Toro-Ankole has lower concentrations than Virunga (Figure 3.5), ranging between 0.0122 and 0.0823 ppm Y.

Virunga olivines C2878, C2797 and C2831 have a wide range of concentrations of the non-metal, P (Figure 3.5). Most Virunga olivines have concentrations between 117 and 138 ppm P, except for C2787, at 61.1 ppm. The Toro-Ankole olivines have a narrower range of P concentrations, between 43.0 and 56.2 ppm.

Ca shows little variation in the Virunga olivines (Figure 3.5), with concentrations between 1280 and 1940 ppm. Ca concentrations in Toro-Ankole occur as two populations (Figure 3.5), with C6098 and C6066 having concentrations of 521 and 509 ppm respectively, while C5619, C5775, C3946 from Toro-Ankole are between 1290 and 1510 ppm. The Toro-Ankole olivines also have a strong negative correlation with Mg# ( $r = -0.76$ )

Alkali metal, Li, has concentrations that are relatively higher in C2831, C2878 and C2797 from Virunga, occurring as two populations, and in a wider range of concentrations than those from the Toro-Ankole field (Figure 3.5). C2831, C2878, C2797, and C2823 from Virunga range between 3.84 and 8.49 ppm Li, except for C2787, at 1.82 ppm Li. The Toro-Ankole olivines have a comparatively narrow range of Li concentrations, between 2.08 and 3.43 ppm Li.

C2831, C2878, C2797 and C2823 from Virunga have a narrow range in concentrations of the alkali metal, Na (Figure 3.5), with most olivines ranging between 52.6 and 61.1 ppm, aside from C2787, at 103 ppm Na. Most Toro-Ankole concentrations are between 77.5 and 115 ppm, while C6066 and C6098 have higher Na concentrations of 198 and 200 ppm respectively.

The post transition metal Al has a relatively narrow range of concentrations in the Virunga olivines (Figure 3.5), with concentrations ranging between 119 and 147 ppm. Toro-Ankole Al concentrations are lower than those in Virunga, ranging between 63.5 and 122 ppm Al.



The remaining elements analysed, Sr, Zr, Nb, Ba, La, Ce, Gd, and Yb, had low and erratic concentrations. Many measurements are below detection limit or are outlier values, hence were not focused on in this study.

### Kalahari

The first-row transition metals, Sc to Zn, in addition to the post-transition metal, Ga, are plotted in (Figure 3.4). Of the transition metals, only Zn ( $r = -0.98$ ) and Mn ( $r = 0.98$ ) have strong negative correlations with Mg# (Figure 3.4). RVK1 has the lowest transition metal concentration of the Kalahari olivines, except for Sc, which is the highest of the Kalahari olivines. LK1 has the highest concentrations for the transition metals from the Kalahari olivines, with the exceptions Sc, Ni and Cr, and with FS4 having the highest Ni and Cr concentrations.

Zn concentrations for the Kalahari olivines range between 55.9 ppm in RVK1, and 93.6 ppm in LK1. RVK1 also has the lowest Mn concentration, at 130 ppm, while LK1, FS1 and FS4 have higher concentrations, at 209, 235 and 241 ppm Mn respectively.

Sc concentrations for Kalahari olivines range between 4.32 and 5.80 ppm. V concentrations vary more than those of Sc. RVK1 has the lowest concentration, at 3.13 ppm V, while the other Kalahari olivines have higher concentrations, with FS1 at 6.44 ppm, FS4 at 6.79 ppm and LK1 the highest V concentration, at 8.02 ppm.

RVK1 has the lowest Ti concentration, at 38.2 ppm, while LK1, FS1 and FS4 have 97.5, 110 and 127 ppm respectively. RVK1 has the lowest Co concentration, at 137 ppm, and LK1 has the highest, at 171 ppm Co. RVK1 also has the lowest Ga concentration, at 0.0409 ppm, while FS1 has 0.133 ppm Ga, FS4 has 0.138 ppm Ga and RVK1 has 0.167 ppm Ga. RVK1 also has the lowest Cu concentration, at 1.15 ppm Cu, while FS1 has 3.50 ppm Cu, FS4 has 3.77 ppm Cu and LK1 has 4.27 ppm Ga.

The non-metal, P, has a limited range of concentrations in the Kalahari olivines (Figure 3.5), between 41.4 and 52.9 ppm. The alkaline earth metal, Ca, has a strong negative correlation with Mg# for the Kalahari olivines ( $r = -0.78$ ), (Figure 3.5). RVK1 has the lowest Ca concentration, at 78.8 ppm, while FS1 has 145 ppm, FS4 has 156 ppm, and LK1 has 172 ppm. With all the Ca concentrations relatively plotting relatively low for the Kalahari olivines (Figure 3.5).

In the Kalahari olivines, the alkali metals, Li and Na, have their lowest concentrations in RVK1. The Kalahari olivines have consistently low Li concentrations (Figure 3.5), ranging between 1.48 and 2.49 ppm. RVK1 has a Na concentration of 60.8 ppm, while the remaining Kalahari olivines have higher concentrations, with FS1 at 127 ppm Na, FS4 at 140 ppm Na, and LK1 at 159 ppm Na. RVK1 also has the lowest concentration of the post-transition metal, Al, at 12.8 ppm, while FS4 has 46.3 ppm Al, FS1 has 42.1 ppm Al and LK1 has 59.8 ppm Al. The second-row transition metal, Y, has low concentrations in the Kalahari olivines (Figure 3.5). The highest olivine average from Kalahari is 0.00617 ppm Y. Zr ranged between 0.07 and 0.237 ppm in Kalahari olivines.

The remaining elements analysed, Sr, Nb, Ba, La, Ce, Gd, and Yb, had low and erratic concentrations. Many measurements are below detection limit or are outlier values, hence were not focused on in this study.

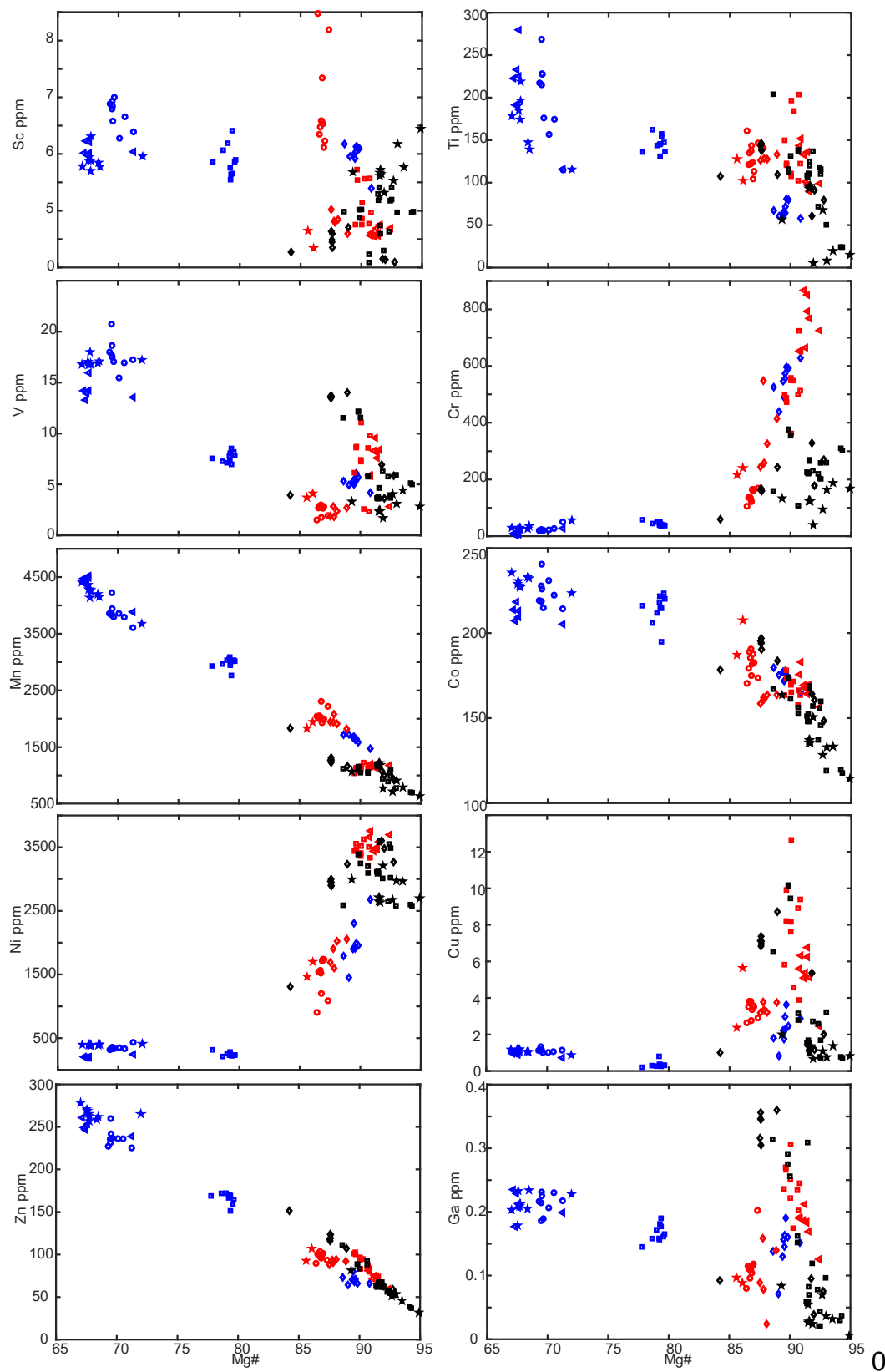


Figure 3.4: LA-ICP-MS analyses of first-row transition metals in addition to the post-transition metal Ga plotted against Mg#. Same key as figure 3.3.

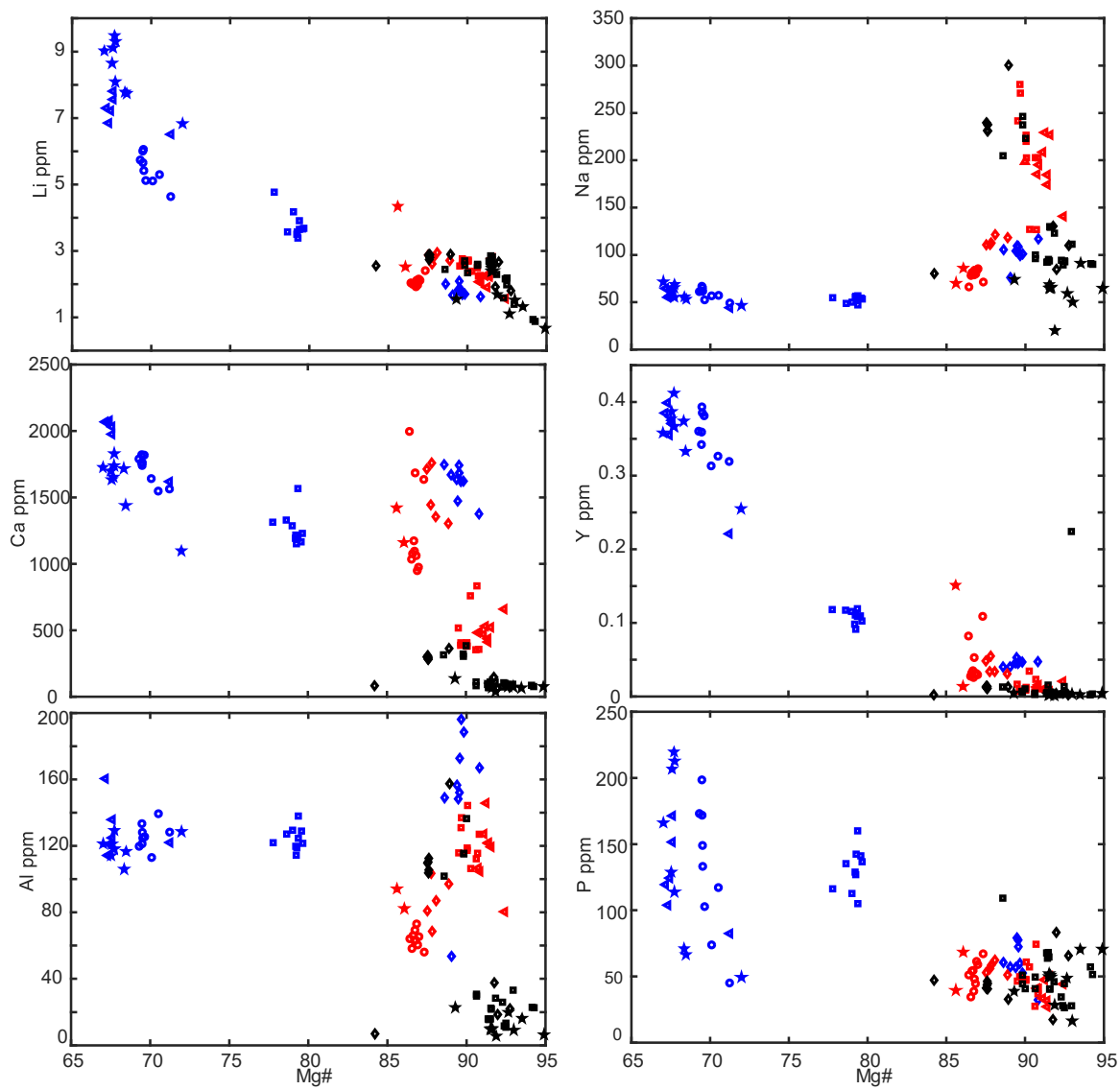


Figure 3.5 LA-ICP-MS analyses of selected elements (Li, Na, Ca, Y, Al and P) against Mg#. Same key as figure 3.3.

Table 2: Averaged LA-ICP-MS olivine analyses in ppm.

	Virunga					Toro-Ankole					Kalahari			
	C2831	C2878	C2797	C2823	C2787	C5619	C5775	C6066	C6098	C3946	FS1	FS4	RVK1	LK1
Li	8.49	5.50	7.08	3.84	1.82	3.43	2.08	2.19	2.47	2.79	2.08	2.49	1.48	2.45
B	10.0	9.00	8.14	21.0	10.6	11.1	16.7	12.5	13.7	12.5	19.5	16.4	21.0	15.0
Na	61.1	59.7	55.0	52.6	103	78.0	77.5	198	200	115	127	140	60.8	159
Al	119	127	127	125	147	88.2	63.5	113	122	87.4	42.1	46.3	12.8	59.8
P	138	136	117	127	61.1	54.0	51.1	43.0	52.6	56.2	52.9	41.4	46.3	48.0
Ca	1660	1720	1940	1280	1610	1290	1370	509	521	1510	145	156	78.8	172
Sc	5.92	6.71	6.10	5.92	5.95	4.49	7.11	4.67	5.19	4.82	5.05	4.65	5.80	4.32
Ti	177	205	197	146	65.9	115	137	117	154	131	110	127	38.2	97.5
V	17.0	18.0	14.0	7.55	5.15	3.93	2.36	6.67	6.76	2.34	6.44	6.79	3.13	8.02
Cr	29.0	23.8	12.2	45.0	543	229	137	703	525	358	235	241	130	209
Mn	4230	3860	4310	2980	1640	1890	2090	1160	1140	1940	1010	1080	870	1210
Co	230	224	210	213	174	197	181	169	168	162	148	162	137	171
Ni	392	344	210	249	2000	1580	1360	3550	3460	1860	2900	3320	2890	2980
Cu	1.10	1.11	0.915	0.351	2.22	4.01	3.28	5.33	7.57	3.45	3.50	3.77	1.15	4.27
Zn	265	236	250	167	70.1	99.8	97.3	76.4	92.1	91.6	68.2	74.6	55.9	93.6
Ga	0.209	0.213	0.205	0.164	0.141	0.0928	0.119	0.186	0.238	0.0979	0.133	0.138	0.0409	0.167
Sr	0.0286	0.0310	0.0237	0.0110	0.0228	0.0220	0.0191	0.0238	0.0277	0.0331	0.0042	0.00239	0.00809	0.00947
Y	0.366	0.352	0.341	0.111	0.0454	0.0823	0.0514	0.0122	0.0158	0.0402	0.0432	0.0052	0.0032	0.00617
Zr	0.197	0.169	0.113	0.0596	0.241	*	0.176	0.256	0.289	0.0519	0.210	0.209	0.0700	0.237
Nb	0.00554	0.0079	0.0126	0.00303	0.00303	0.0137	0.00432	0.00376	0.00976	0.00753	0.116	0.0564	0.0612	0.147
Ba	0.0307	0.0243	0.0396	0.0138	0.0349	0.0112	0.0168	0.00638	0.00742	0.0219	0.0152	0.0120	0.0179	0.0131
La	0.0712	0.0422	0.0427	0.00717	0.0370	0.0162	0.00465	0.0112	0.0264	0.00335	0.00371	0.00138	0.00300	0.00218
Ce	0.610	0.450	0.772	0.0166	0.453	0.223	0.0516	0.00852	0.0530	0.00789	0.0221	0.00269	0.00299	0.00201
Gd	0.0214	0.0165	0.0202	0.0112	0.0147	0.0251	0.00826	0.00671	0.00425	0.0152	0.0119	0.00893	0.0116	0.0107
Yb	0.111	0.109	0.0983	0.0319	0.0106	0.0164	0.0196	0.00380	0.00429	0.0117	0.0271	0.00581	0.00819	0.00652

\* = All values for that sample rejected

## 4. Discussion

---

In the following section the results of individual olivine spot analyses from this study are combined with spot analyses from other western branch volcanic olivine samples, from Foley et al. (2011), in a series of discrimination plots. These discrimination plots compare these olivines to selected olivine analyses and fields from other authors.

### 4.1 Fractionation

There is a wide range of Mg# represented by the olivines of this study (Figure 4.1). Spot analyses from Virunga samples have Mg# between 67.0 and 90.8, from Toro-Ankole spot analyses have Mg# between 85.6 and 92.4, and Kalahari spot analyses Mg# range between 84.2 and 94.9. Assuming a normal fractionation relationship between a peridotite source and its melt, olivines with Mg# <88 are associated with having undergone fractionation processes (Neumann et al., 1999). However, this may not apply to the alkaline rock compositions of this study (Foley et al., 2011). Olivines from the Virunga field have Mg# <88, except for the ugandite, C2787, and therefore have likely undergone fractionation. However, most of the olivines from Toro-Ankole have Mg# ≥88, except for the katungite, C5775, and the leucite ankaratrite, C5619, which have Mg# <88 (Figure 4.1).

A fractionation relationship has already been established between ugandite and ankaratrite, where removal of 35 % of the olivine from a ugandite melt forms ankaratrite compositions (Tappe et al., 2003). This fractionation relationship correlates with calculated fractionation paths caused by the removal of olivine from a range of melts (8-20 % MgO), from an initial peridotite end member (grey field in Figure 4.1) (Herzberg, 2011, Søager et al., 2015). However, as the high MgO contents of the rock types of this study are expected to have lower olivine/melt partition coefficients for Ni, according to Herzberg (2011) they should have a shallower gradient than the magma evolution path of Figure 4.1 (grey field), as seen in the high MgO olivines from continental arcs (Figure 4.1). The discrepancy between the predicted and observed fractionation path is accounted for, as the olivine/melt partition coefficient for Ni is 5-6 times higher in alkaline melts compared to non-alkaline melts, with alkaline melts having  $D_{Ni}$  values of 30–90 (Foley et al., 2013). As a result, the high MgO alkaline rocks of this study have olivine fractionation paths similar to those expected of low MgO, non-alkaline rocks.

Kimberlite fractionation usually corresponds to a decrease in Ni without an associated decrease in Mg# (blue crosses Figure 4.1) (Brett et al., 2009, Bussweiler et al., 2015), due

to the digestion fractional crystallization (DFC) process consuming pyroxene during transport (Bussweiler et al., 2015). A single olivine from the Kalahari kimberlite samples has a Mg# <88 (grain 4 from LK1, with a Mg# of ~84). This olivine grain is unusual in that it appears to follow a normal fractionation path of a mutual decrease in Ni and Mg# (Bussweiler et al., 2015), and as an outlier, this may just be a xenocryst.

Only cores were measured in the remaining Kalahari olivines and there was no obvious decrease in Ni, hence no obvious fractionation, which is consistent with the mantle xenocrystic (Figure 4.1) trend of Bussweiler et al. (2015). The DFC trend cannot be ruled out for the Kalahari olivines, though may be impossible to observe due to the ubiquitous degree of rim alteration present in the Kalahari kimberlite olivines.

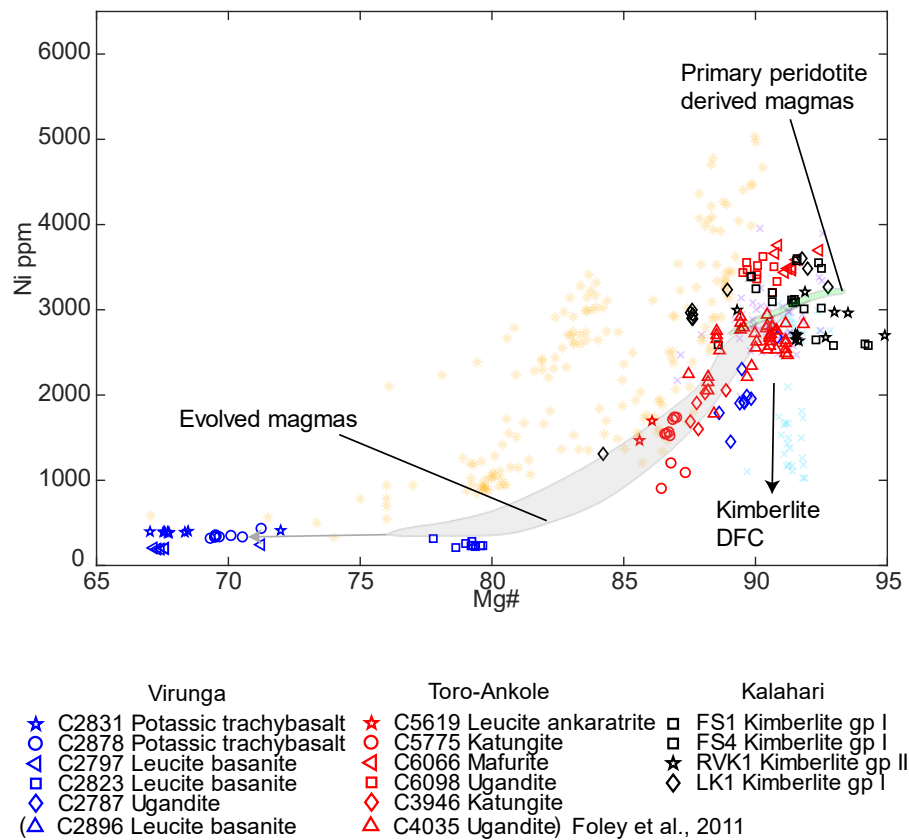


Figure 4.1: Mg# vs Ni of olivine spot analyses, modified from Herzberg, (2011), Søager et al., (2015) and Bussweiler et al. (2015). Primary peridotite derived magma field ranging in composition from 8-38% MgO (green), and the evolution path of melts ranging in composition from 8-20% MgO (grey), calculated by Herzberg, (2011).

Key presented for the analyses of this study in addition to the relevant analyses from Foley et al., (2011), data coloured by location with Virunga olivines in blue, Toro-Ankole olivines in red, and Kalahari olivines in black. Reference data: Continental arcs- (★) (Wade et al., 2006, Straub et al., 2008) kimberlites – (x) (Brett et al., 2009, De Hoog et al., 2010, Bussweiler et al., 2015), peridotite xenoliths – (x) (Kaesler et al., 2006, De Hoog et al., 2010).

Fe/Mn ratios are not expected to change due to olivine fractionation alone (Figure 4.3), with the ratio remaining constant as Mg# decreases (Sobolev et al., 2007, Herzberg, 2011). A wide variety of Fe/Mn ratios are present in the Toro-Ankole and Kalahari samples (Figure 4.3), with the ratio inherited from the melt source (Sobolev et al., 2007). The Fe/Mn ratio is expected to slightly increase when pyroxene and olivine are fractionated from the magma (Søager et al., 2015). Pyroxene and olivine fractionation from a melt with an olivine composition similar to that of the Virunga ugandite, C2787, could potentially produce the Fe/Mn values of the olivines observed in the Virunga leucite basanite, C2823. These Fe/Mn values are possible because the olivines are spatially and temporally associated. The remaining low Mg# olivines from Virunga, potassic trachybasalts C2831 and C2878, and leucite basanite, C2797, have similar Fe/Mn values to that of the higher Mg# leucite basanite, C2823. It is likely that these samples (C2831, C2878 and C2797) have undergone further fractionation of olivine only, from a melt with an olivine Fe/Mn composition similar to the leucite basanite, C2823 (Figure 4.3). Differing fractionating phases are supported petrographically, as the leucite basanite, C2823, has olivine as its main phenocryst phase, potentially indicating the removal of clinopyroxene. Contrary to this, the potassic trachybasalts C2831 and C2878, and leucite basanite, C2797, have clinopyroxene as their main phenocryst phase, potentially indicating the removal of olivine.



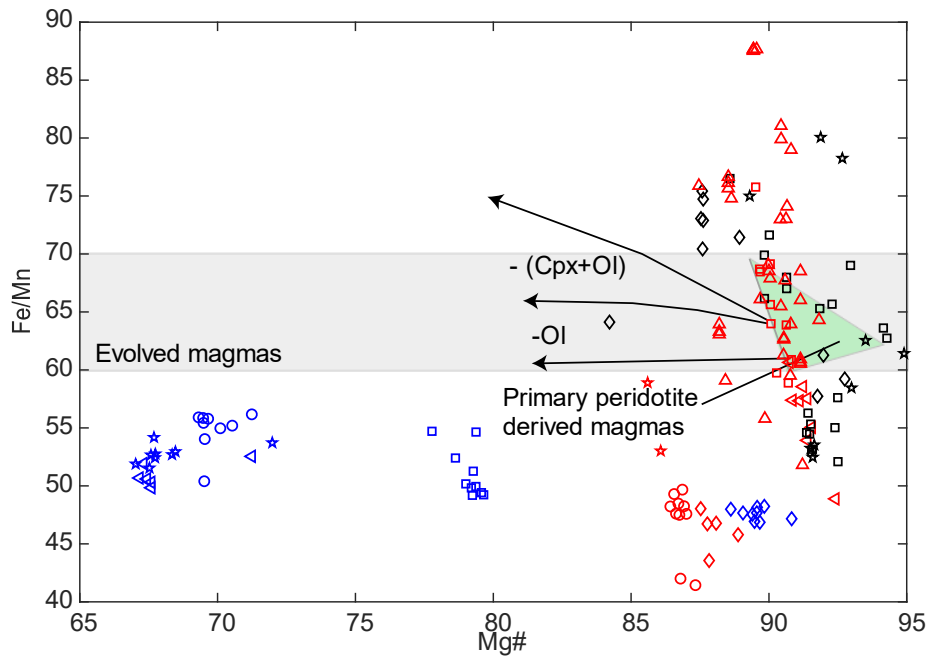


Figure 4.2: Mg# vs Fe/Mn of olivine spot analyses: Modified from Herzberg, (2011) and Søager et al., (2015).  $-(\text{Cpx}+\text{Ol})$  = fractionation path from removal of clinopyroxene and olivine,  $-\text{Ol}$  = fractionation path from the removal of olivine alone. Primary peridotite derived magma field ranging in composition from 8-38% MgO (green), and the evolution path of melts ranging in composition from 8-20% MgO (grey), calculated by Herzberg, (2011). Key same as Figure 4.1.

The fractionation of pyroxene decreases Ca concentrations in olivine due to the increased compatibility of Ca in pyroxene relative to olivine (Søager et al., 2015), while fractionation of olivine increases Ca concentrations in the remaining olivines (Herzberg, 2011, Søager et al., 2015). If the Virunga magma initially had a starting composition that would crystallize olivines, similar to the composition of the olivines in the ugandite, C2787 (Figure 4.4), then the fractionation path was initially dominated by pyroxene to form the composition of the olivines in C2823. This was likely followed by olivine fractionation to produce the remaining olivine compositions (C2831, C2878 and C2797) of the Virunga population.

The Toro-Ankole olivines appear to have only minor fractionation relative to that of Virunga, indicated by their higher Mg# (Figure 4.4). The leucite ankaratrite, C5619, is an exception due to it having Ca compositions indicative of olivine fractionation from ugandite, consistent with previous research on the formation of this rock type (Tappe et al., 2003). The mafurite, C6066, and the ugandite, C6098, from Toro-Ankole, have olivine Ca

concentrations and Mg# which fall within the range of mantle values (Figure 4.4) (Herzberg, 2011), while the ugandite, C4035, has a wider range of Ca concentrations, some of which fall within the mantle range. These samples from Toro-Ankole are the most primitive from the western branch of the East African Rift System. South African olivine melilitites that are similar in whole rock composition to the katungites of this study (Day et al., 2014) (Figure 4.4) appear to follow a different fractionation path relative to the Toro-Ankole olivines, with the South African olivine melilitites dominated by pyroxene fractionation. All the olivines from the western branch of the East African Rift System measured in this study have Mg# and Ca concentrations outside that expected of primary peridotite magmas and their fractionation products (Søager et al., 2015).

The kimberlite olivines of the Kalahari samples have Mg# and Ca concentrations all falling within the values for mantle olivines (Herzberg, 2011). Kimberlites (Figure 4.4) from other studies (Brett et al., 2009, De Hoog et al., 2010, Bussweiler et al., 2015) also fall within the mantle trend, except for the melt trend illustrated by Bussweiler et al., (2015), which has elevated Ca concentrations. These elevated Ca concentrations associated with kimberlite melts are not seen in the kimberlite olivines of this study.

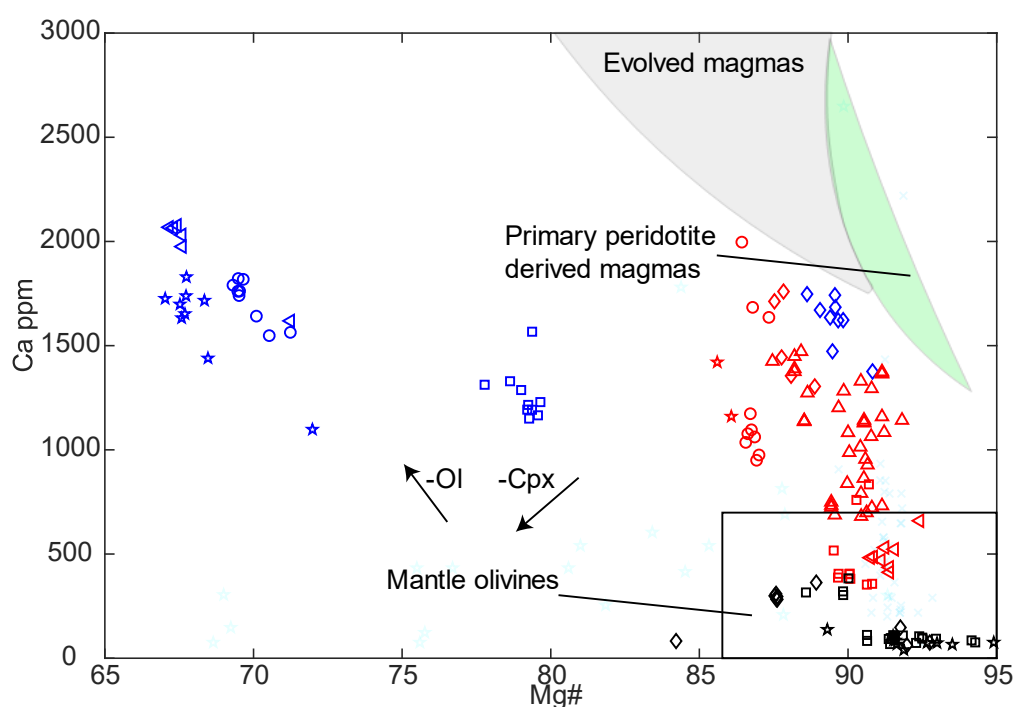


Figure 4.3: Mg# vs Ca of olivine spot analyses, Modified from Herzberg, (2011) and Søager et al., (2015). Primary peridotite derived magma field ranging in composition from 8-38% MgO (green), and the evolution path of melts ranging in composition from 8-20% MgO (grey), calculated by Herzberg, (2011). Reference data: Kimberlites – (x) (Brett et al., 2009, De Hoog et al., 2010, Bussweiler et al., 2015), South African melilitites (☆) (Day et al., 2014). Key same as Figure 4.1.

Ni and Co in olivine can be decoupled from each other, either by mantle melting in the presence of pyroxenite, raising the Ni/Co ratio, or via fractional crystallization that lowers the Ni/Co ratio (Sobolev et al., 2007, Foley et al., 2013). This results in the Ni/Co of olivines deviating from the primitive earth value of Ni/Co = 20 (Figure 4.4) (Sobolev et al., 2007). Melting of a pyroxenite, formed via the recycling of oceanic crust, is evidenced in the elevated the Ni/Co of Hawaiian OIB, with values well over the Earth average of 20 (in this case, Ni/Co up to 30) (Figure 4.4) (Sobolev et al., 2007). Recycling of continental crust extremely elevates Ni/Co (up to 90) of Mediterranean lamproites, likely due to melting of phlogopite (which has a Ni/Co value up to 35) in the source, with high Ni/Co (up to 35) (Figure 4.4) (Foley et al., 2013). Fractional crystallization causes the Ni/Co ratio to drop below the Earth average of 20 (Sobolev et al., 2007), likely due to crystallization of phases such as Cr-spinel, which have Ni/Co values of 4, as seen in aillikites (Figure 4.4) (Veter et al., 2017).

The Virunga olivines from C2823, C2831, C2878 and C2797, except for the ugandite, C2787, all have extremely low Ni/Co <5 (Figure 4.4), which is consistent with the fractionation indicated by Ni, Mg#, Fe/Mn and Ca in the previous sections. The Virunga olivines appear to have a steeper Ni/Co fractionation path than the non-alkaline, Hawaii OIB (Sobolev et al., 2007) or arc volcanics (Wade et al., 2006). This is likely due to the high  $D_{Ni}$  (30–90) of olivine in alkaline melts compared to non-alkaline melts ( $D_{Ni}$  5-35) (Foley et al., 2013), while the partition coefficient of olivine in alkaline leucite basanites is similar to non-alkaline melts such as Kilauea basalts ( $D_{Co}$  ~4) (Foley et al., 2011). This suggests olivine as a significant (but not the only), fractionating phase in the Virunga olivines. The ugandite, C2787, has Ni/Co values ranging from 8-16, and at similar Mg# to aillikites (Figure 4.4) (Veter et al., 2017), suggesting the involvement of the fractionation of Cr-spinel. Cr-spinel fractionation in the C2787 olivines is indicated by them being depleted in Cr (Figure 4.5).

The Toro-Ankole olivines from C5619, C5775, and C3946, as well as the majority of analyses from C4035, have Ni/Co values ranging 5-20, hence have likely been subject to some degree of fractionation (Sobolev et al., 2007). These values and gradient, relative to Mg#, are similar to that of aillikites, which indicates the involvement of Cr-spinel fractionation (Figure 4.4) (Veter et al., 2017). This is supported by the depletion in Cr relative to the other Toro-Ankole olivines, C6066 and C6098 (Figure 4.4). The olivines from C6066 and C6098 mostly have Ni/Co values  $\geq 20$ , with most values being ~20-21. As the Ni/Co values for the C6066 and C6098 olivines are not drastically above the Earth

average of 20, in contrast to Hawaiian OIB (Sobolev et al., 2007) and Mediterranean lamproites (Foley et al., 2013), it would not be appropriate to use the Ni/Co ratio alone as an indicator of recycled crustal material. However, the Ni/Co ratio does indicate that fractionation was not a significant process in the C6066 and C6098 olivines, which agrees with the fact that they are within the Mg# vs Ca mantle olivine range (Figure 4.3).

Kalahari olivines mostly have Ni/Co values slightly above the Earth average of 20, and are similar to that of diamond inclusions (Sobolev et al., 2009) (Figure 4.4). LK1 has the lowest Ni/Co of the Kalahari olivines, with several spot analyses of Ni/Co at ~15, correlating with the low Mg# of the samples (Figure 4.4). Grain 4 from LK1 has the lowest Kalahari Mg#, at ~84, and also has the lowest Ni/Co value of the Kalahari olivines, at ~7, and overall appears to be an outlier (Figure 4.4). The Ni/Co values do not correlate with the Mg# vs Ca mantle olivine field in Figure 4.3. The Kalahari olivines do not follow the DFC fractionation path of a kimberlite melt trend (Bussweiler et al., 2015).

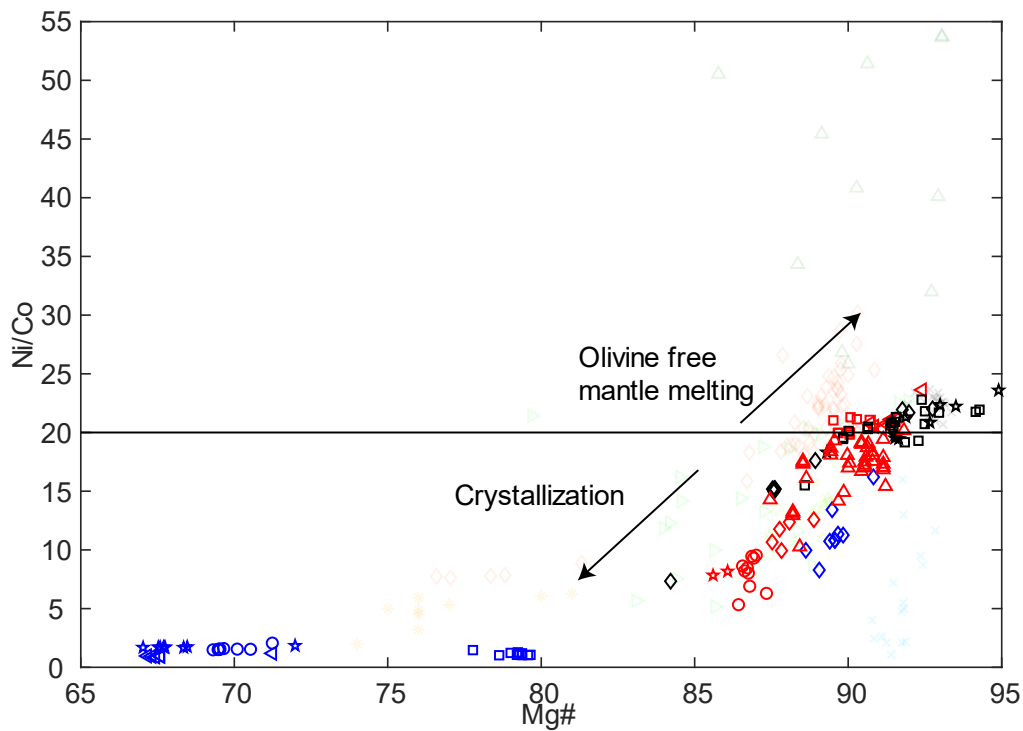


Figure 4.4: Mg# vs Ni/Co of olivine spot analyses. Modified from Sobolev et al., (2007) and Foley et al., (2013). Line at Ni/Co 20 is representative of the average value from the bulk silicate Earth, core, and mantle (McDonough and Sun, 1995). Values above the line have Ni/Co ratios indicative of mantle melting with the involvement of pyroxenite and values below the line indicative of fractional crystallization (Sobolev et al., 2007).

Reference data: Kimberlites – (x) (Brett et al., 2009, De Hoog et al., 2010, Bussweiler et al., 2015), Continental arc- (★)(Wade et al., 2006), aillikites –(△)(Veter et al., 2017), Mediterranean lamproites-(△)(Prelević and Foley, 2007, Prelević et al., 2013), diamond inclusions-(x)(Sobolev et al., 2009), Hawaii OIB- (◇) (Hagerty et al., 2006, Sobolev et al., 2007). Key same as Figure 4.1.

Melts derived from continental peridotites lacking a recycled crustal material component crystallize olivines with a limited range of Mn concentrations ( $1000 \pm 300$  ppm) (Figure 4.5), while exhibiting a variety of Cr concentrations (Veter et al., 2017), which is seen in the kimberlite melt trend (Bussweiler et al., 2015) and the Baffin Island picrites (De Hoog et al., 2010). A positive correlation between Mn and Cr is associated with the melting of “dry” pyroxenite, defining the oceanic trend in Figure 4.5 (Veter et al., 2017). A decrease in Mn alone is associated with fractionation (Sobolev et al., 2007), and Mn has a strong negative correlation with Mg# for all the samples in this study (Figure 3.4).

The leucite basanite, C2896, is the only sample from Virunga to have olivine Mn and Cr concentrations within the continental peridotite band (Figure 4.5). C2896 is another potentially unfractionated starting composition for the trachybasalts and basanites from Virunga samples C2823, C2831, C2878, and C2797. Unfortunately, Mg# data for the olivines of this sample are not available, hence cannot be effectively checked for other fractionation properties. Another possibility is that C2896 represents heterogeneity in the source. Holmes and Harwood (1937) noted that although C2896 has a groundmass characteristic of a leucite basanite, the sample shared more features in common with leucite ankaratrite/ugandite. Gathering major element data on the olivines from C2896, as well as a greater spread of olivines from the sample, would be recommended to help resolve this and rule out possibilities such as the olivine samples by Foley et al. (2011) being xenocrystic.

Relative to C2896, the ugandite, C2787, has a decrease in Cr with an increase in Mn, a trend similar to that of aillikites (Figure 4.5) (Veter et al., 2017), which suggests the involvement of fractionated Cr-spinel. The leucite basanite, C2823, appears to also follow this aillikite-like trend (Figure 4.5), implying further fractionation involving Cr-spinel. The remaining trachybasalts and basanite from Virunga in C2831, C2878 and C2797 have elevated Mn with no increase in Cr, ruling out Mn enrichment from a “dry” pyroxenite source for these samples (Veter et al., 2017).

Half of the Toro-Ankole samples, C4035, C6066 and C6098, have olivine Mn and Cr concentrations within the continental peridotite band (Figure 4.5). The other half of the Toro-Ankole samples, C5619, C5775 and C3946, have enrichment in Mn and depletion in Cr, making fractionation involving Cr-spinel likely, and ruling out Mn enrichment from a “dry” pyroxenite (Veter et al., 2017).

The Kalahari olivine Mn and Cr concentrations are mostly within the continental peridotite band (Figure 4.5), and correspond to the typical mantle trend (Veter et al., 2017). They also have lower Cr, though overlapping Cr values with the kimberlite melts compiled by Bussweiler et al. (2015), and substantially lower Cr (Figure 4.5) than Baffin Island picrites (De Hoog et al., 2010).

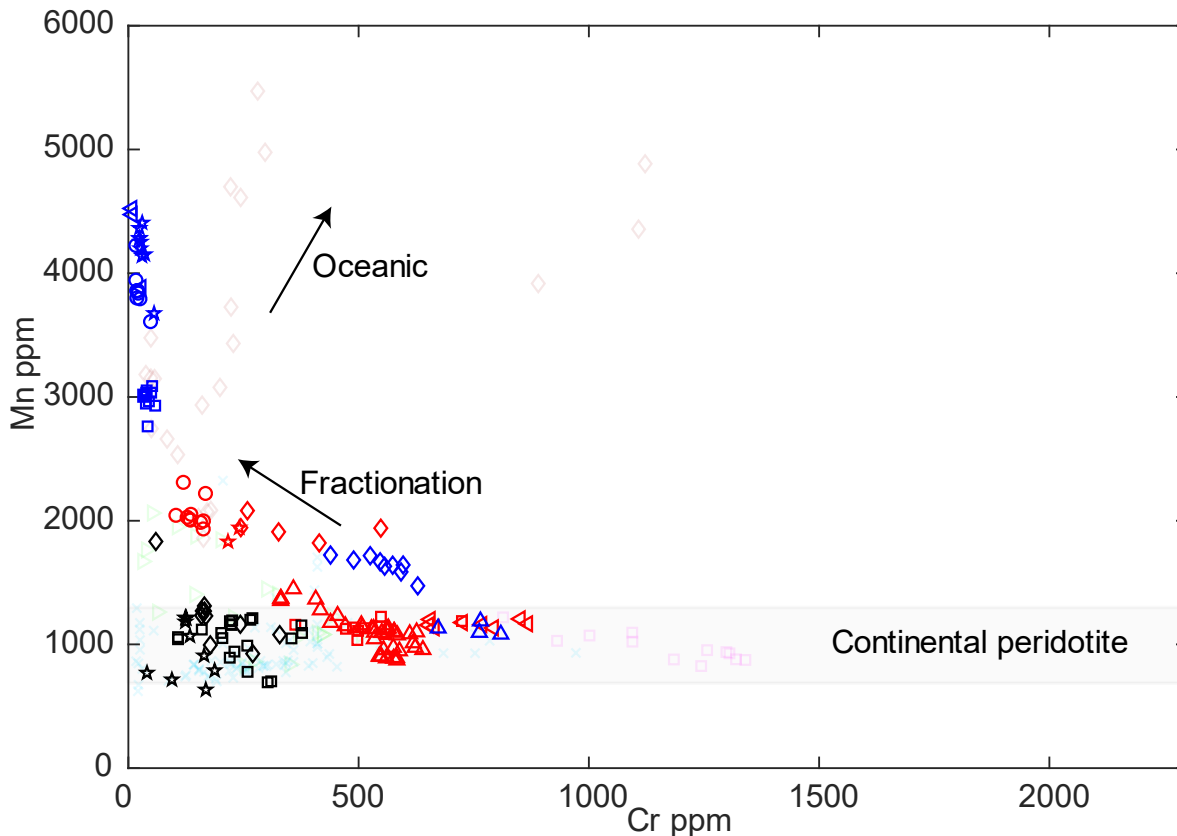


Figure 4.5: Cr vs Mn of olivine spot analyses. Modified from Veter et al., (2017). Continental peridotite field (grey) defined by  $1000 \pm 300$  ppm Mn and variable Cr concentration (Veter et al., 2017). Fractionation trend illustrated by decreasing Cr and increasing Mn. Oceanic trend illustrated by a mutual increase in Mn and Cr. Reference data: Canary Islands-( $\blacklozenge$ ) (Neumann et al., 1999), Aillikites-( $\blacktriangle$ ) (Veter et al., 2017), Kimberlites-( $\times$ ) (Brett et al., 2009, De Hoog et al., 2010, Bussweiler et al., 2015), Baffin Island picrite-( $\blacksquare$ ) (De Hoog et al., 2010). Key same as Figure 4.1.

#### 4.2 Source composition

Deviation from mantle concentrations of Ni (2500 ppm) against Co (140 ppm), Sc (3.5 ppm), Al (100 ppm), and Mn (1000 ppm) can be used to discriminate between the recycling of oceanic and continental material (Foley et al., 2013). The “Oceanic” trend results from the recycling of oceanic crust, which subsequently reacts with the existing peridotitic mantle to form an olivine free pyroxenite, partially melting to form OIB magmas (Sobolev et al., 2007, Foley et al., 2013). The “Orogenic” trend results from the recycling of

continental sedimentary material, which also reacts with the mantle to form an olivine free pyroxenite source, but includes significant phlogopite (Foley et al., 2013, Veter et al., 2017) or amphibole veining (Foley et al., 2013).

The “Oceanic” trend presents itself as a mutual increase of Ni, with Co, Sc, Al, and Mn relative to mantle values, similar to Canary OIB (Figure 4.6) (Neumann et al., 1999, Foley et al., 2013). This enrichment in Ni only, with Co, Sc, Al and Mn remaining near mantle values, is characteristic of recycled continental sedimentary material, and is evident in Mediterranean lamproites (Figure 4.6) as the “Orogenic” trend (Prelević and Foley, 2007, Foley et al., 2013).

The ugandite, C2787, and leucite basanite, C2896, olivine concentrations plot at the base of the “Orogenic” trend for Co, Sc, and Mn, though do not exceed mantle Ni concentrations (Figure 4.6). An exception to this is Al vs Ni, in which C2896 has elevated Al relative to mantle concentrations and plots at the base of the “Oceanic” trend, though is not considered a strong signal of either an “Oceanic” or “Orogenic” trend, as the signal is not present in multiple elements.

The trachybasalts and basanites from Virunga, C2823, C2831, C2878, and C2797, do not plot well on this discrimination plot (Figure 4.6), as they all have very low Ni due to fractionation (See previous section 4.1). C2823, C2831, C2878, and C2797 have slightly elevated Co, Sc, Mn, and Al relative to mantle values. Co and Mn have correlations with Mg#, therefore it is likely that these elevations are the effects of fractionation and not of the source assemblage. Sc and Al are not severely affected by fractionation (See Figure 3.3 and 3.4), if Ni concentrations for C2823, C2831, C2878, and C2797, are “reconstructed” to the hypothetical pre-fractionation Ni concentration of the ugandite C2787, they would have values in close proximity.

All Toro-Ankole olivines plot at the base of the “Orogenic” trend (Figure 4.6), though only the katungite, C6066, and the ugandites, C6098 and C4035, have higher than mantle Ni concentrations (Foley et al., 2013). It is possible that these olivines have a phlogopite-bearing pyroxenite component in their source. The remainder of the Toro-Ankole olivines, C3946, C5775 and C5619, have Ni concentrations below that of mantle olivines (Foley et al., 2013), and are not considered to have strong signals of either the “Orogenic” or the “Oceanic” trends (Veter et al., 2017).

All Kalahari olivines have Ni concentrations slightly above the mantle average (Foley et al., 2013), except for the single fractionated olivine in LK1 (grain 4). Co, Sc, and Mn concentrations are generally above mantle values, while Al is depleted relative to the mantle for most Kalahari olivines (Figure 4.6) (Foley et al., 2013). Kalahari olivines generally plot at the base of the “Orogenic” trend, possibly indicating a phlogopite-bearing pyroxenite component in their source (Foley et al., 2013).

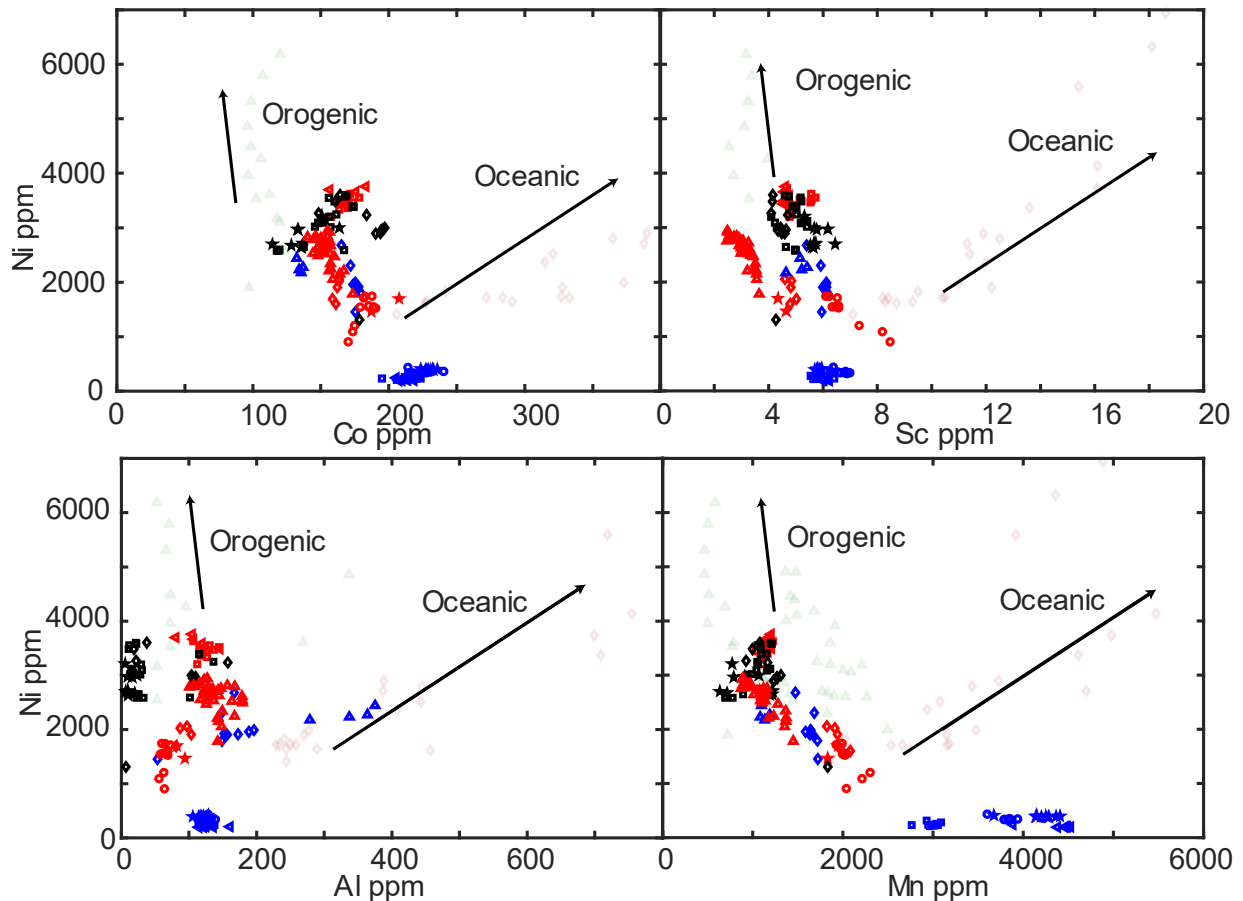


Figure 4.6: Co, Sc, Al, and Mn vs Ni. Modified from Foley et al., (2013). Oceanic trend indicates the involvement of pyroxenite in the source as inferred from OIB data (Neumann et al., 1999, Foley et al., 2013). Orogenic trend indicates involvement of phlogopite-pyroxenite or amphibole-pyroxenite in the source as inferred from Mediterranean lamproites (Prelević and Foley, 2007, Foley et al., 2013).

Reference data: Canary Islands-( $\diamond$ ) (Neumann et al., 1999), Mediterranean lamproites-( $\triangle$ )(Prelević and Foley, 2007, Prelević et al., 2013). Key same as Figure 4.1.

Olivine Mn/Fe values have little change with fractionation (Figure 4.2) (Herzberg, 2011), and have been used in conjunction with Ni/Mg to estimate the proportion of pyroxenite in the source (Sobolev et al., 2007). Ni/Mg is elevated in olivine-free pyroxenite sources, as Ni is over three times more compatible in olivine than pyroxene, and has the highest Ol/Opx ratio of any of the transition metals (Foley et al., 2013). Due to this difference in compatibility, when a pyroxenite source re-melts, Ni will preferentially enter the early



crystallizing olivine phase rather than entering the source, elevating the Ni/Mg ratio (Sobolev et al., 2007). For the same compatibility reasons, Mn/Fe is lower in olivines that crystallize from a pyroxenite source, as the mineral/melt partition coefficient of Mn/Fe is 0.82 for olivine, 1.12 for orthopyroxene, and 1.25 for clinopyroxene (Foley et al., 2013).

This simple pyroxenite-peridotite member solution works best for mid ocean ridge basalts (MORB) and Hawaii OIB, with MORB having 10-30 % pyroxenite in the source, and Hawaii OIB having ~60 % pyroxenite in their source (Sobolev et al., 2007). When different types of mafic volcanics are taken into consideration, more end members must be added to the discrimination diagram. Aillikite volcanism requires phlogopite and carbonate in its source, causing aillikite olivines to have lower Mn/Fe (Veter et al., 2017), tending towards phlogopite xenocryst values (Mn/Fe at 0.01 and Ni/Mg at 0.08) (Fritschle et al., 2013).

Virunga olivines C2823, C2831, C2878 and C2797 have very low Ni/Mg and high Mn/Fe (Figure 4.7). Ni/Mg is fractionation sensitive, with removal of Ni from melt during olivine fractionation (Sobolev et al., 2007), and as such Ni/Mg is unlikely to be a good indicator of the pyroxenite content in the source. However, the Mn/Fe contents being high are indicative of a peridotite source. The relatively unfractionated olivines of C2787 have low Ni/Mg and high Mn/Fe (Figure 4.7), indicating a peridotite rich source (Sobolev et al., 2007). The C2787 Mn/Fe vs Ni/Mg values primarily plot within the low end of the Mediterranean leucitite concentrations (Figure 4.6), which are thought to have elevated Mn/Fe values due to the presence of carbonate metasomatic fluids (Ammannati et al., 2016). The presence of carbonate metasomatism in the Virunga olivines is unlikely, as the associated Ca elevations, of >2300 ppm (Ammannati et al., 2016), are not present in the Virunga samples (Figure 4.3). However, it is possible that carbonate metasomatism is a factor, and the high Ca signature is masked at higher pressures (Veter et al., 2017).

Toro-Ankole olivines have a much wider spread of Mn/Fe vs Ni/Mg (Figure 4.7). The olivines of the ugandite, C4035, have the largest spread of Mn/Fe values (Figure 4.7). The lowest of these values overlaps with the aillikites of Veter et al, (2017), tending towards a phlogopite xenocryst composition (Fritschle et al., 2013), and indicating that this may be a phase present in the source. Most of C4035 olivines have concentrations closer to the peridotite field, along with the olivines from C6066 and C6098 (Figure 4.7), though still having Mn/Fe lower than the peridotite field, which indicates the partial presence of pyroxenite in the source (Sobolev et al., 2007). C5775 and C3946 have low Ni/Mg and high Mn/Fe, with concentrations in the lower end of the leucitites field, overlapping with the

olivines of the Virunga sample, C2787 (Figure 4.7). The elevated Mn/Fe in C5775 and C3946 may be due to carbonate metasomatism (Ammannati et al., 2016), though as with the Virunga sample, the elevated Ca signal is absent, however again may be masked at higher pressures (Veter et al., 2017).

The Kalahari olivines primarily plot near the peridotite field, though with lower Mn/Fe concentrations (Figure 4.7) indicating the partial presence of pyroxenite in the source (Sobolev et al., 2007). Two spot analyses of the RVK1 olivines (Grain 3 and 4) approach the Mn/Fe vs Ni/Mg composition of aillikites, hence may have a phlogopite component in their source (Veter et al., 2017).

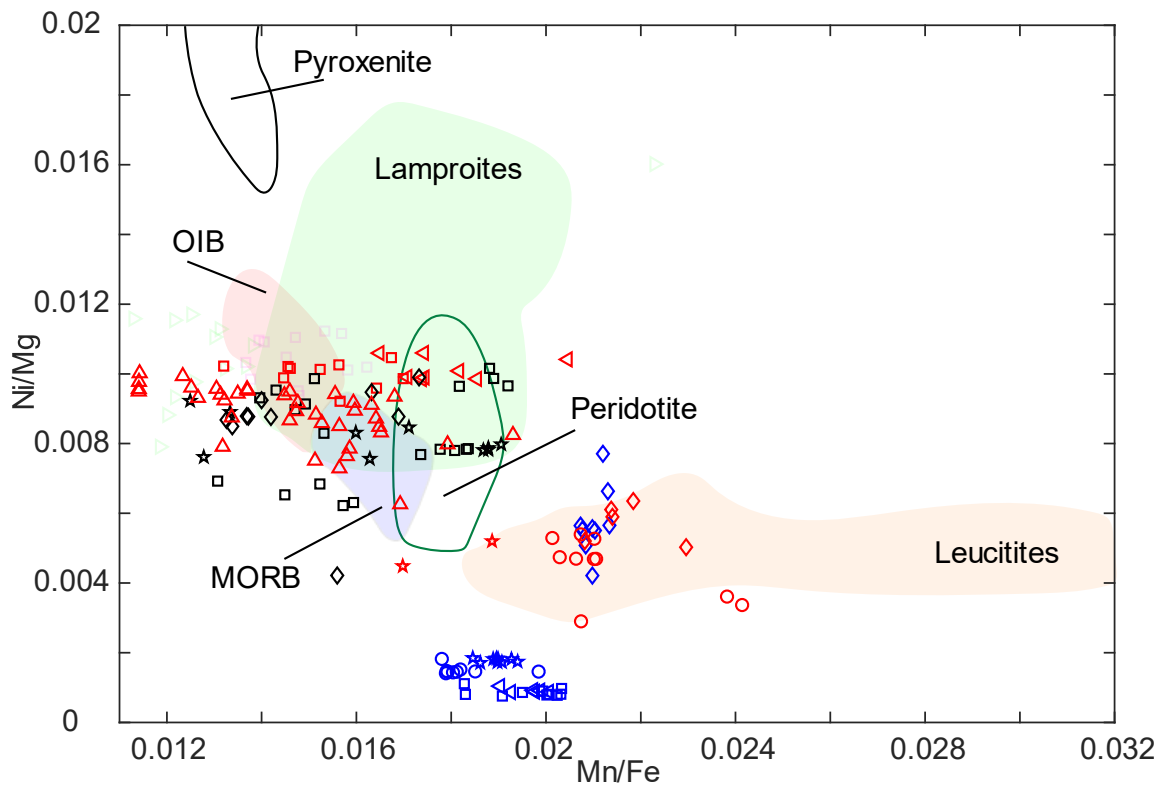


Figure 4.7: Mn/Fe vs Ni/Mg. Modified from Sobolev et al., (2007) and Ammannati et al., (2016). Fields from Ammannati et al., (2016) and references therein. Low Mn/Fe and high Ni/Mg is associated with the presence of pyroxenite in the source (Sobolev et al., 2007). Extremely low Mn/Fe can be caused by the presence of phlogopite in the source (Veter et al., 2017) and high Mn/Fe from carbonate metasomatism of the source (Ammannati et al., 2016). Reference data: Aillikites-( $\blacktriangleright$ ) (Veter et al., 2017), Baffin Island picrite-( $\square$ ) (De Hoog et al., 2010). Key same as Figure 4.1.

Li is enriched in the Earth's crust ( $30 \pm 3.6$  ppm) (Sauzéat et al., 2015) relative to typical mantle-derived olivines, that contain  $<3$  ppm Li (Seitz and Woodland, 2000, Jeffcoate et al., 2007, De Hoog et al., 2010). Li enrichment is present in post-collisional Mediterranean lamproites (up to 45 ppm), and these Li enrichments (Figure 4.8) are associated with the input of recycled continental crustal material via subduction that is subsequently stored in

the subcontinental lithospheric mantle (Prelević et al., 2013). An enriched Li signature is not always present in lamproite olivines, for example West Kimberly lamproites only have slight enrichment in Li (up to 6 ppm), with any extreme enrichment in Li likely diffusing back into the mantle over time (Jaques and Foley, 2017).

The ugandite, C2787, and the leucite basanite, C2896, have Li concentrations above that expected for typical mantle olivines (<3 ppm) (Figure 4.8) (Seitz and Woodland, 2000, Jeffcoate et al., 2007, De Hoog et al., 2010). The remaining Virunga olivines, C2823, C2831, C2878, and C2797, have Li concentrations above the typical mantle-derived maximum value of 3 ppm (Figure 4.8).

The amount of Li enrichment has a correlation with fractionation ( $\text{Li}\uparrow$ ,  $\text{Mg}\#\downarrow$ ) (Figure 3.4 and 4.1 to 4.3). Olivine is moderately incompatible with Li (De Hoog et al., 2010), however it is still the main reservoir phase of Li in the mantle (Ammannati et al., 2016). Olivine is likely the main fractionating phase of the Virunga melts, therefore a decrease in concentration with fractionation would be expected. Varying degrees of crustal contamination could explain the Li variation of the Virunga samples, and this effect could be further enhanced by the heterogeneity of the Li concentration in the crust (Sauzéat et al., 2015).

All Toro-Ankole and Kalahari olivines have Li concentrations in the mantle range (Figure 4.8), aside from the Toro-Ankole sample, C5619, which had one spot analysis with a Li value of 4.3 ppm, though another spot analysis on the same grain returned a value of 2.5 ppm. Further investigation into Li zoning in these olivines would be prudent.

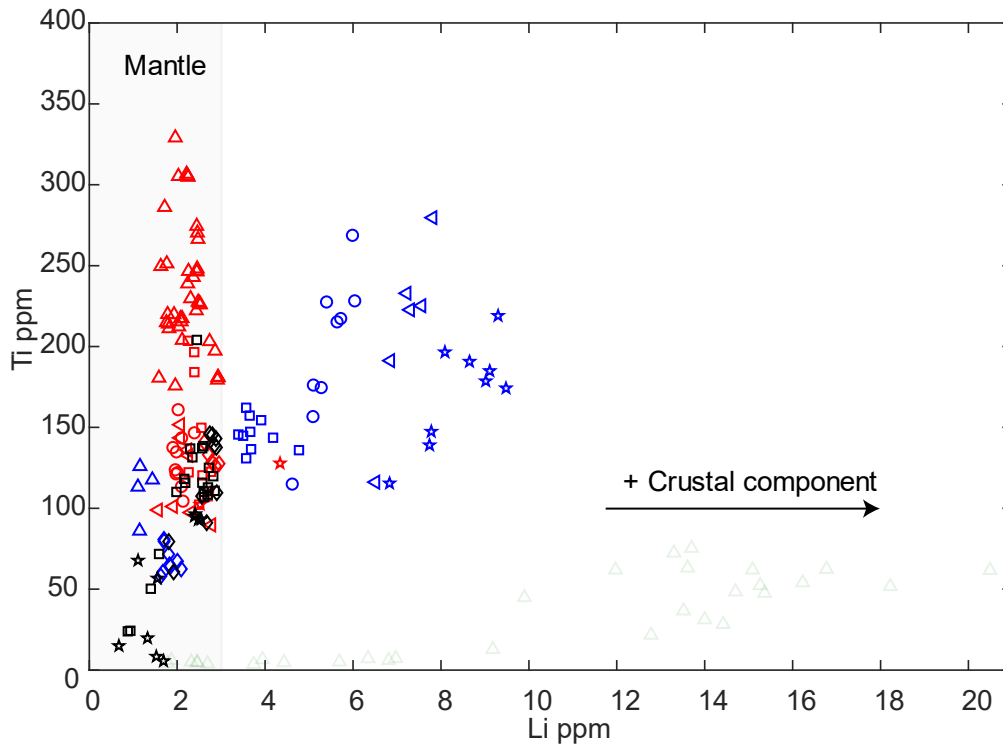


Figure 4.8: Li vs Ti. Modified from Ammannati et al., (2016). Mantle band defined by Li <3 ppm and varying Ti concentrations (Foley et al., 2013, Veter et al., 2017). Addition of crustal component evidenced by Mediterranean lamproites in the form of recycled subducted continental crustal material Prelević et al., (2013). Reference data: Mediterranean lamproites-( $\triangle$ ), (Prelević et al., 2013), Key same as Figure 4.1.

Olivines from the Kalahari kimberlites mostly exhibit characteristics of primary mantle compositions (Figure 4.3, 4.5, 4.8), and the sampled grain cores have not undergone DFC processes associated with a kimberlite melt trend (Figure 4.1), though this process cannot be ruled out for the unmeasured rims of these grains (Bussweiler et al., 2015). It is likely that they represent xenocrystic mantle olivines collected during the kimberlites ascent (Brett et al., 2009, Bussweiler et al., 2015).

Olivine is the most common mineral in the upper mantle, and the upper mantle is mostly peridotitic in composition (McDonough and Rudnick, 1998), therefore a reasonable assumption is that the olivine xenocrysts in the Kalahari samples were from a peridotite. Spinel peridotites, garnet peridotites, and garnet spinel peridotites can be distinguished from each other using Mn vs log Al, and log Zr vs Sc plots (Figure 4.9) (De Hoog et al., 2010). These plots exploit trace element partition coefficient differences between spinel and garnet, and/or between phases that exist in the same fields as spinel or garnet (De

Hoog et al., 2010). Mn and Sc partition into garnet over olivine or spinel (De Hoog et al., 2010), which lowers the Mn and Sc concentration in the remaining olivine.

Al partitioning is temperature and pressure dependent (Bussweiler et al., 2017), with increased partitioning into olivine at lower temperatures and pressures where spinel is stable (De Hoog et al., 2010). The Zr partitioning mechanism is less clear. Zr may be more compatible in olivine at high pressure, while at low pressure may be less compatible, or a phase co-existing with spinel may have an affinity for Zr (De Hoog et al., 2010).

Using the log Zr vs Sc discrimination (Figure 4.9), all the Kalahari olivines have Sc and Zr concentrations within the spinel peridotite field. This corresponds with the Mn vs Al concentrations, where most of the Kalahari olivines fall within the spinel lherzolite field. A few spot analyses from RVK1 and FS1 plot within other fields and are likely spinel harzburgites, as this allows the four discrimination elements to agree with each other. Spinel peridotites occur at lower pressures and temperatures, corresponding to depths <100 km (Winter, 2010), therefore the olivines in the Kalahari samples are likely sampling subcontinental lithospheric mantle (Griffin et al., 2003).

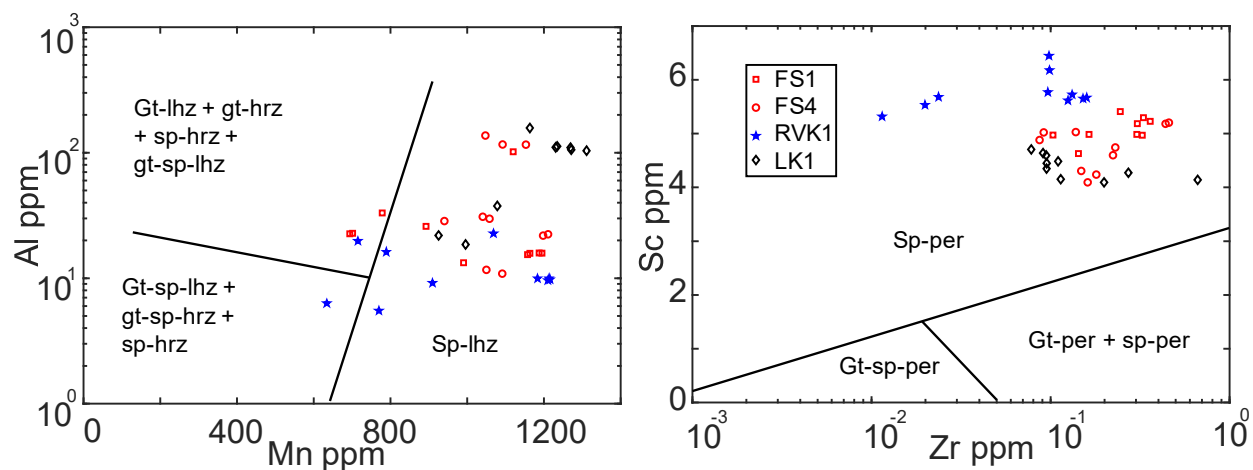


*Figure 4.9 Mn vs log Al and log Zr vs Sc. Modified from De Hoog et al., (2010). Discriminatory plots taking advantage of partition coefficients between olivine, garnet, and spinel as well as temperature and pressure effects (De Hoog et al., 2010). New key used for this plot.*

In reducing conditions, V and Sc both have a 3<sup>+</sup> valence state and have similar compatibilities with olivine ( $D_V$  0.09,  $D_{Sc}$  0.23) (Foley et al., 2013). In oxidizing conditions, Sc retains its 3<sup>+</sup> valence, while V attains a 5<sup>+</sup> valence that reduces its compatibility with olivine (Mallmann and O'Neill, 2009). This allows the V/Sc ratio to be used as a proxy for the oxidizing conditions during olivine crystallization (Veter et al., 2017). Care must be taken when using this ratio, as V and Sc are compatible with garnet ( $D_V$  1.7,  $D_{Sc}$  2.7) and clinopyroxene ( $D_V$  1.3,  $D_{Sc}$  1.4), and can distort the ratio (Foley et al., 2013). Phlogopite is enriched in V (40-170 ppm) relative olivines (2-10 ppm), while phlogopite has similar Sc concentrations (3-10 ppm) to olivines (4-12 ppm) (Fritschle et al., 2013). If phlogopite is present in the magma source, V/Sc can be elevated without a change in system oxidation (Fritschle et al., 2013).

Peridotite xenoliths have a limited Ni concentration range and a large variation in V/Sc (grey field, Figure 4.1) (Kaesler et al., 2006, De Hoog et al., 2010), consistent with peridotite xenoliths being sampled from a range of depths and a decrease in oxygen fugacity with depth (Woodland and Koch, 2003).

Virunga olivines have V/Sc ratios up to 3.2, this is lower than Canadian aillikites which inherit their high elevated V/Sc ratio from phlogopite in the source (Veter et al., 2017) though higher than Mediterranean lamproites (Prelević and Foley, 2007) (Figure 4.10). The Virunga olivines from C2831, C2878, and C2797 from Virunga have elevated V/Sc (2.15-3.1) compared to the other Virunga olivines (C2823 and C2787) potentially indicating lower oxygen fugacity in these samples (Foley et al., 2013). C2831, C2878, and C2797 could have had their V/Sc ratio distorted as clinopyroxene is the main phenocryst phase in these samples (Foley et al., 2011).

In the Toro-Ankole olivines, the ugandite, C4035, has the highest V/Sc, at 2.8 (Figure 4.10). C4035 also has the lowest Mn/Fe from the field (Figure 4.7). Low Mn/Fe is associated with phlogopite in the source (Veter et al., 2017), and it is likely that the high V/Sc in C4035 is due to compositional variation and not a redox variation. The remaining Toro-Ankole olivines have low V/Sc, at <2.5.

LK1 has the highest V/Sc of the Kalahari olivines, at 3.1. LK1 is likely to be a spinel lherzolite (Figure 4.9), as the V/Sc values will not have been distorted by garnet. LK1 has a moderately low Mn/Fe (Figure 4.7), hence a potential phlogopite component that could raise the V/Sc value (Veter et al., 2017). LK1 also has Ni/Mg close to that of OIB (Figure 4.7), from which a pyroxenite component in the source could alter the V/Sc value

(Foley et al., 2013). Though LK1 olivines may have formed in a source with a lower oxygen fugacity relative to the other kimberlites of this study (Foley et al., 2013), with the remaining Kalahari olivines have low V/Sc, at <2.5. This could be a reflection of LK1 overlying the Zimbabwe craton while FS1, FS4, and RVK1 overlying the Kaapvaal craton (Griffin et al., 2003, Field et al., 2008).

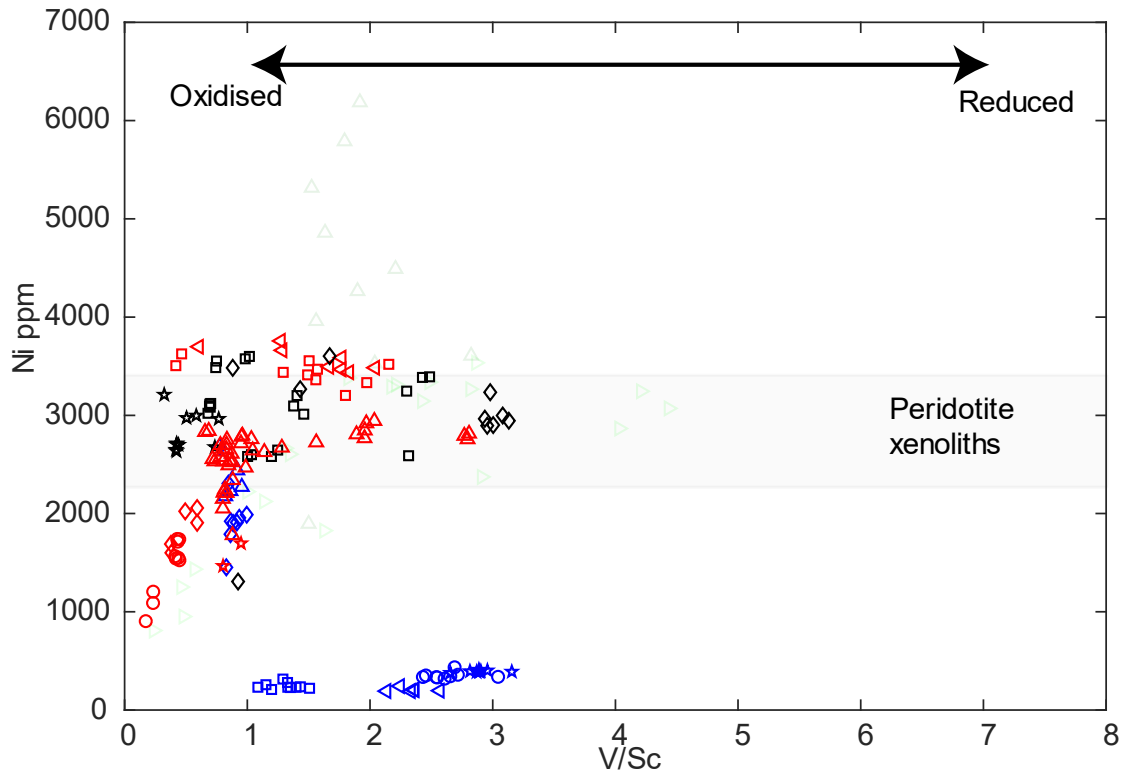


Figure 4.10: V/Sc vs Ni. Modified from Veter et al., (2017). V/Sc can potentially be used as a proxy for the redox state of the system, with high V/Sc indicating reducing conditions and Low V/Sc indicating oxidized conditions. Peridotite field constructed from values from Kaeser et al. (2006) De Hoog et al., (2010). Reference data: Aillikites-(<math>\blacktriangleright</math>) (Veter et al., 2017), lamproites- (<math>\triangle</math>). Key same as Figure 4.1.

## **5. Conclusions**

---

### **5.1 Western branch East African Rift System**

The Virunga olivines show a clear fractionation trend (Figures 4.1 to 4.5), with the temporally and spatially related ugandite C2787 being a candidate for the pre-fractionation melt composition (Figure 4.1 to 4.5). The fractionation path is defined by initial fractionation of both olivine and clinopyroxene, followed by the dominate fractionation of olivine (Figure 4.1 to 4.3). A possible control on this sequence of fractionation is pressure dependence, with clinopyroxene preferentially fractionating at higher pressures (Johnson et al., 1989). The most fractionated Virunga olivines are also enriched in Li due to interaction with a crustal component (Figure 4.8).

The Virunga olivine trace element data are consistent with recent whole rock data from the nearby Visoke volcano that also has evidence of at least two different mantle sources. These include a primary mantle source forming ugandites and a fractionated source forming leucite basanites. In addition to this there is evidence of crustal contamination in the leucite basanites in the form of quartz and rutile xenoliths (Muravyeva et al., 2017).

The olivines of kamafugites from Toro-Ankole present as two populations with one being representative of primary mantle and the other showing a slight degree of fractionation (Figure 4.1, 4.4 and 4.5). This population split is also reflected in Mn/Fe ratios with the primary mantle population likely having component of pyroxenite in its source while the slightly fractionated population potentially having undergone carbonate metasomatism (Figure 4.7). One Toro-Ankole ugandite from the primary mantle population has very low Mn/Fe that is indicative of phlogopite in its source. This ugandite also has elevated V/Sc which would usually be indicative of a lower oxygen fugacity (Figure 4.10), however it is more likely that this elevated ratio is not related to redox conditions but due to V enrichment from phlogopite.

These data are consistent with the whole rock data of Rosenthal et al., (2009), with their study concluding the presence of two main metasomatic assemblages, one carbonate rich and one phlogopite rich. They also noted the dominance of pyroxenite xenoliths in the area. The conclusions of this study for the samples from the western branch of the East African Rift are summarised in Figure 5.1.



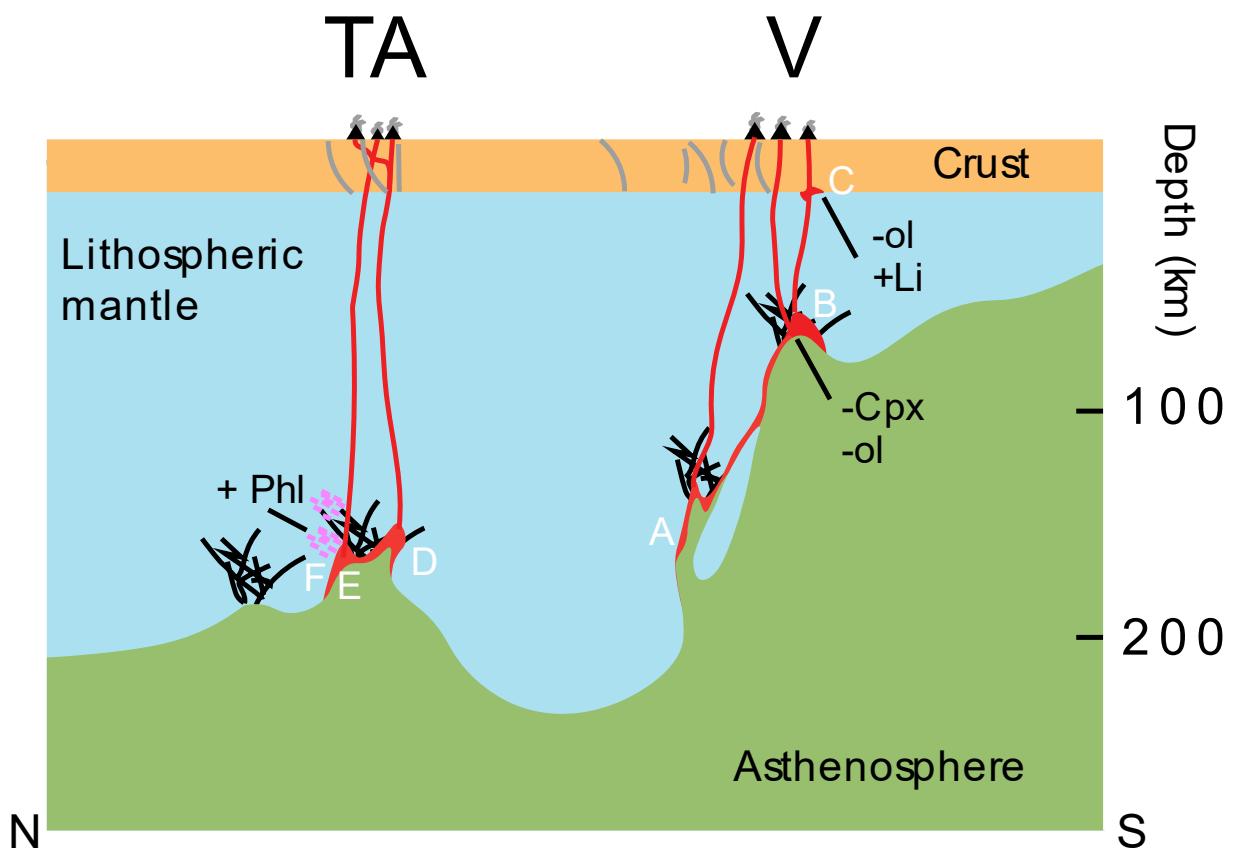


Figure 5.1: A summary of the western branch of the East African Rift System. TA= Toro-Ankole V= Virunga. A= potential primary kamafugitic source of the Virunga field. B = magmas derived from clinopyroxene and olivine fractionation. C= magmas derived from olivine fractionation and elevated Li from crustal contamination. D= slightly fractionated kamafugitic source that has undergone carbonate metasomatism E= unfractionated kamafugitic source F = kamafugitic source that has undergone phlogopite metasomatism or interaction.

## **5.2 Kalahari craton**

The Kalahari craton olivines are xenocrystic in the measured cores (Figure 4.1). These xenocrysts are mostly spinel lherzolites with a few spinel harzburgites, and likely were entrained by the kimberlite magma within the sub-continental lithospheric mantle (Figure 4.9). The main distinction between the LK1 kimberlite that overlies the Zimbabwe craton and the remaining FS1, FS4, and RVK1 kimberlites is the V/Sc contents of their olivines with LK1 values being elevated. However, it is not clear whether these elevations are the result of a reduction in oxygen fugacity relative to the other kimberlites or due to compositional differences in their source (Figure 4.10).

## **5.3 Future directions**

Future directions for research that were outside the scope of a ten month masters project are as follows: Gathering larger datasets by utilising SELFRAG to increase LA-ICP-MS and EMP/SEM throughput in order to aid quantifying variation within samples and the identification of xenocryst populations (Brandl et al., 2015). Developing a protocol for tuning a LA-ICP-MS for an olivine specific matrix using a synthetic olivine standard or blank as has been done for other minerals (Gilbert et al., 2017), and so as to reduce interferences such as SiO on Sc (Foley et al., 2011). SEM imaging the olivines measured in this study would be useful to quantify the presence of zoning as has been done in other studies (Bussweiler et al., 2017, Veter et al., 2017).

## References:

---

- ALLSOPP, H. & BARRETT, D. 1975. Rb/ Sr age determinations on South African kimberlite pipes. *Physics and Chemistry of the Earth*, 9, 605-617.
- ALLSOPP, H., NICOLAYSEN, L. & HAHN-WEINHEIMER, P. 1968. Rb/K ratios and Sr-isotopic compositions of minerals in eclogitic and peridotitic rocks. *Earth and Planetary Science Letters*, 5, 231-244.
- AMMANNATI, E., JACOB, D. E., AVANZINELLI, R., FOLEY, S. F. & CONTICELLI, S. 2016. Low Ni olivine in silica-undersaturated ultrapotassic igneous rocks as evidence for carbonate metasomatism in the mantle. *Earth and Planetary Science Letters*, 444, 64-74.
- BARIFAIJO, E., MUWANGA, A. & SCHUMANN, A. 2010. Geochemistry of the potassic basalts from the Bufumbira volcanic field in southwestern Uganda. *Tanzania Journal of Science*, 36.
- BEGG, G., GRIFFIN, W., NATAPOV, L., O'REILLY, S. Y., GRAND, S., O'NEILL, C., HRONSKY, J., DJOMANI, Y. P., SWAIN, C. & DEEN, T. 2009. The lithospheric architecture of Africa: Seismic tomography, mantle petrology, and tectonic evolution. *Geosphere*, 5, 23-50.
- BORST, A. 2012. The formation and modification of the sub-cratonic lithospheric mantle beneath Botswana.
- BOYD, F. & PASTERIS, J. 1978. Ilmenite association at the Frank Smith kimberlite pipe, South Africa. *Carnegie Inst. Wash., Ybk*, 77, 866-870.
- BRANDL, P. A., GENSKE, F. S., BEIER, C., HAASE, K. M., SPRUNG, P. & KRUMM, S. H. 2015. Magmatic Evidence for Carbonate Metasomatism in the Lithospheric Mantle underneath the Ohře (Eger) Rift. *Journal of Petrology*, 56, 1743-1774.
- BRETT, R., RUSSELL, J. & MOSS, S. 2009. Origin of olivine in kimberlite: Phenocryst or impostor? *Lithos*, 112, 201-212.
- BUSSWEILER, Y., BREY, G., PEARSON, D., STACHEL, T., STERN, R., HARDMAN, M., KJARSGAARD, B. & JACKSON, S. 2017. The aluminum-in-olivine thermometer for mantle peridotites—Experimental versus empirical calibration and potential applications. *Lithos*, 272, 301-314.
- BUSSWEILER, Y., FOLEY, S. F., PRELEVIĆ, D. & JACOB, D. E. 2015. The olivine macrocryst problem: new insights from minor and trace element compositions of olivine from Lac de Gras kimberlites, Canada. *Lithos*, 220, 238-252.
- CLARKE, D. & PE-PIPER, G. 1983. Multiply exsolved clinopyroxene megacrysts from the Frank Smith mine, Cape province, South Africa. *Lithos*, 16, 75-84.
- CLARKE, D., PE, G., MACKAY, R., GILL, K., O'HARA, M. & GARD, J. 1977. A new potassium-iron-nickel sulphide from a nodule in kimberlite. *Earth and Planetary Science Letters*, 35, 421-428.
- COMBE, A. 1937. The Katunga volcano, south-west Uganda. *Geological Magazine*, 74, 195-200.
- COMBE, A. D. & HOLMES, A. 1945. *The kalsilite-bearing lavas of Kabirenge and Lyakauli, south-west Uganda*, Oliver and Boyd.
- COMBE, A. D. & SIMMONS, W. C. 1933. *The volcanic area of Bufumbira, Part I: The Geology of the Volcanic Area of Bufumbira, South-West Uganda*, Government Printer, South Africa.
- CONDOMINES, M., CARPENTIER, M. & ONGENDANGENDA, T. 2015. Extreme radium deficit in the 1957 AD Mugogo lava (Virunga volcanic field, Africa): Its bearing on olivine-melilitite genesis. *Contributions to Mineralogy and Petrology*, 169, 29.
- DAVIS, G. 1977. The ages and uranium contents of zircons from kimberlites and associated rocks. *Carnegie Institution of Washington Yearbook*, 76, 631-654.

- DAY, J. M., PETERS, B. J. & JANNEY, P. E. 2014. Oxygen isotope systematics of South African olivine melilitites and implications for HIMU mantle reservoirs. *Lithos*, 202, 76-84.
- DE HOOG, J. C., GALL, L. & CORNELL, D. H. 2010. Trace-element geochemistry of mantle olivine and application to mantle petrogenesis and geothermobarometry. *Chemical Geology*, 270, 196-215.
- DE MULDER, M., HERTOGEN, J., DEUTSCH, S. & ANDRÉ, L. 1986. The role of crustal contamination in the potassic suite of the Karisimbi Volcano (Virunga, African Rift Valley). *Chemical Geology*, 57, 117-136.
- DEER, W. A., HOWIE, R. A. & ZUSSMAN, J. 1992. *An introduction to the rock-forming minerals*, Longman Scientific & Technical Hong Kong.
- DEINES, P. & HARRIS, J. 2004. New insights into the occurrence of  $^{13}\text{C}$ -depleted carbon in the mantle from two closely associated kimberlites: Letlhakane and Orapa, Botswana. *Lithos*, 77, 125-142.
- DEINES, P., HARRIS, J. & GURNEY, J. 1987. Carbon isotopic composition, nitrogen content and inclusion composition of diamonds from the Roberts Victor kimberlite, South Africa: Evidence for  $^{13}\text{C}$  depletion in the mantle. *Geochimica et Cosmochimica Acta*, 51, 1227-1243.
- EBINGER, C. 1989. Tectonic development of the western branch of the East African rift system. *Geological Society of America Bulletin*, 101, 885-903.
- EBY, G. N., LLOYD, F. E. & WOOLLEY, A. R. 2009. Geochemistry and petrogenesis of the Fort Portal, Uganda, extrusive carbonatite. *Lithos*, 113, 785-800.
- EBY, G. N., LLOYD, F. E., WOOLLEY, A. R., STOPPA, F. & WEAVER, S. 2003. Geochemistry and mantle source (s) for carbonatitic and potassic lavas, western branch of the East-African Rift System, SW Uganda. *Geolines*, 15, 23-27.
- EXLEY, R. 1982. Cr-rich spinel and garnet in two peridotite xenoliths from the Frank Smith mine South Africa: Significance of Al and Cr distribution between spinel and garnet. *Mineralogical Magazine*, 45, 129-34.
- FIELD, M., STIEFENHOFER, J., ROBEY, J. & KURSZLAUKIS, S. 2008. Kimberlite-hosted diamond deposits of southern Africa: a review. *Ore Geology Reviews*, 34, 33-75.
- FOLEY, S., VENTURELLI, G., GREEN, D. & TOSCANI, L. 1987. The ultrapotassic rocks: characteristics, classification, and constraints for petrogenetic models. *Earth-Science Reviews*, 24, 81-134.
- FOLEY, S. F., JACOB, D. E. & O'NEILL, H. S. C. 2011. Trace element variations in olivine phenocrysts from Ugandan potassic rocks as clues to the chemical characteristics of parental magmas. *Contributions to Mineralogy and Petrology*, 162, 1-20.
- FOLEY, S. F., LINK, K., TIBERINDWA, J. V. & BARIFAIJO, E. 2012. Patterns and origin of igneous activity around the Tanzanian craton. *Journal of African Earth Sciences*, 62, 1-18.
- FOLEY, S. F., PRELEVIC, D., REHFELDT, T. & JACOB, D. E. 2013. Minor and trace elements in olivines as probes into early igneous and mantle melting processes. *Earth and Planetary Science Letters*, 363, 181-191.
- FOURNELLE, J. 2011. An Investigation of "San Carlos Olivine": Comparing USNM-distributed Material with Commercially Available Material. *Microscopy and Microanalysis*, 17, 842.
- FRICK, C. 1973. Intergrowths of orthopyroxene and ilmenite from Frank Smith Mine, near Barkly West, South Africa. *South African Journal of Geology*, 76, 195-200.
- FRITSCHLE, T., PRELEVIĆ, D., FOLEY, S. F. & JACOB, D. E. 2013. Petrological characterization of the mantle source of Mediterranean lamproites: Indications from major and trace elements of phlogopite. *Chemical Geology*, 353, 267-279.

- FURMAN, T. 1995. Melting of metasomatized subcontinental lithosphere: undersaturated mafic lavas from Rungwe, Tanzania. *Contributions to Mineralogy and Petrology*, 122, 97-115.
- GILBERT, S., OLIN, P., THOMPSON, J., LOUNEJEVA, E. & DANYUSHEVSKY, L. 2017. Matrix dependency for oxide production rates by LA-ICP-MS. *Journal of Analytical Atomic Spectrometry*, 32, 638-646.
- GOLDSTEIN, J. I., NEWBURY, D. E., ECHLIN, P., JOY, D. C., LYMAN, C. E., LIFSHIN, E., SAWYER, L. & MICHAEL, J. R. 2003. *Scanning Electron Microscopy and X-ray Microanalysis*.
- GRIFFIN, W., O'REILLY, S. Y., NATAPOV, L. & RYAN, C. 2003. The evolution of lithospheric mantle beneath the Kalahari Craton and its margins. *Lithos*, 71, 215-241.
- GRIFFIN, W., POWELL, W., PEARSON, N. & O'REILLY, S. 2008. GLITTER: data reduction software for laser ablation ICP-MS. *Laser Ablation-ICP-MS in the earth sciences. Mineralogical association of Canada short course series*, 40, 204-207.
- GURNEY, J. J., HARRIS, J. W. & RICKARD, R. S. 1984. Minerals Associated with Diamonds from the Roberts Victor Mine. In: KORNPROBST, J. (ed.) *Developments in Petrology*. Elsevier.
- HAGERTY, J. J., SHEARER, C. K., VANIMAN, D. T. & BURGER, P. V. 2006. Identifying the effects of petrologic processes in a closed basaltic system using trace-element concentrations in olivines and glasses: Implications for comparative planetology. *American Mineralogist*, 91, 1499-1508.
- HERZBERG, C. 2011. Identification of source lithology in the Hawaiian and Canary Islands: Implications for origins. *Journal of Petrology*, 52, 113-146.
- HIGAZY, R. A. 1954. Trace elements of volcanic ultrabasic potassic rocks of southwestern Uganda and adjoining part of the Belgian Congo. *Geological Society of America Bulletin*, 65, 39-70.
- HOLMES, A. 1937. The petrology of katungite. *Geological Magazine*, 74, 200-219.
- HOLMES, A. 1942. A suite of volcanic rocks from south-west Uganda containing kalsilite (a polymorph of  $\text{KAlSiO}_4$ ). *Mineral. Mag*, 26, 217.
- HOLMES, A. 1945. Leucitized granite xenoliths from the potash-rich lavas of Bunyaruguru, Southwest Uganda. *Am. J. Sci.*, 243, 313-332.
- HOLMES, A. 1950. Petrogenesis of katungite and its associates. *Am. Mineralogist*, 35, 772-792.
- HOLMES, A. 1952. The Potash Ankaratrite-Meleleucocitite Lavas of Nabagando and Mbuga Craters, south-west Uganda. *Transactions of the Edinburgh Geological Society*, 15, 187-213.
- HOLMES, A. & HARWOOD, H. F. 1937. *The Volcanic Area of Bufumbira: The Petrology of the Volcanic Field of Bufumbira, South-West Uganda*, Geolog. Survey.
- HUANG, J.-X., GRÉAU, Y., GRIFFIN, W. L., O'REILLY, S. Y. & PEARSON, N. J. 2012. Multi-stage origin of Roberts Victor eclogites: progressive metasomatism and its isotopic effects. *Lithos*, 142, 161-181.
- JACOB, D. 2004. Nature and origin of eclogite xenoliths from kimberlites. *Lithos*, 77, 295-316.
- JACOB, D. E. & FOLEY, S. F. 1999. Evidence for Archean ocean crust with low high field strength element signature from diamondiferous eclogite xenoliths. *Lithos*, 48, 317-336.
- JAQUES, A. & FOLEY, S. 2017. Insights into the petrogenesis of the West Kimberley lamproites from trace elements in olivine. *11th International Kimberlite Conference Botswana*.

- JEFFCOATE, A., ELLIOTT, T., KASEMANN, S., IONOV, D., COOPER, K. & BROOKER, R. 2007. Li isotope fractionation in peridotites and mafic melts. *Geochimica et Cosmochimica Acta*, 71, 202-218.
- JOCHUM, K. P., BRUECKNER, S. M., NOHL, U., STOLL, B. & WEIS, U. 2009. Geostandards and Geoanalytical Research bibliographic review 2008. *Geostandards and Geoanalytical Research*, 33, 501-505.
- JOCHUM, K. P., WEIS, U., STOLL, B., KUZMIN, D., YANG, Q., RACZEK, I., JACOB, D. E., STRACKE, A., BIRBAUM, K. & FRICK, D. A. 2011. Determination of reference values for NIST SRM 610–617 glasses following ISO guidelines. *Geostandards and Geoanalytical Research*, 35, 397-429.
- JOHNSON, R. W., KNUTSON, J. & TAYLOR, S. R. 1989. *Intraplate volcanism: in eastern Australia and New Zealand*, Cambridge University Press.
- KAESER, B., KALT, A. & PETTKE, T. 2006. Evolution of the lithospheric mantle beneath the Marsabit volcanic field (northern Kenya): constraints from textural, P–T and geochemical studies on xenoliths. *Journal of Petrology*, 47, 2149-2184.
- KAMENETSKY, V. S., KAMENETSKY, M. B., SOBOLEV, A. V., GOLOVIN, A. V., DEMOUCHEY, S., FAURE, K., SHARYGIN, V. V. & KUZMIN, D. V. 2007. Olivine in the Udachnaya-East kimberlite (Yakutia, Russia): types, compositions and origins. *Journal of Petrology*, 49, 823-839.
- KISEEVA, E. S., KAMENETSKY, V. S., YAXLEY, G. M. & SHEE, S. R. 2017. Mantle melting versus mantle metasomatism—“The chicken or the egg” dilemma. *Chemical Geology*, 455, 120-130.
- KOEHN, D., LINDENFELD, M., RÜMPKER, G., AANYU, K., HAINES, S., PASSCHIER, C. & SACHAU, T. 2010. Active transsection faults in rift transfer zones: evidence for complex stress fields and implications for crustal fragmentation processes in the western branch of the East African Rift. *International Journal of Earth Sciences*, 99, 1633-1642.
- KUSKY, T. M. 1998. Tectonic setting and terrane accretion of the Archean Zimbabwe craton. *Geology*, 26, 163-166.
- LE BAS, M. 1973. A norm for feldspathoidal and melilitic igneous rocks. *The Journal of Geology*, 81, 89-96.
- LINK, K., KOEHN, D., BARTH, M. G., TIBERINDWA, J. V., BARIFAIJO, E., AANYU, K. & FOLEY, S. F. 2010. Continuous cratonic crust between the Congo and Tanzania blocks in western Uganda. *International Journal of Earth Sciences*, 99, 1559-1573.
- LLOYD, F. 1981. Upper-mantle metasomatism beneath a continental rift: clinopyroxenes in alkali mafic lavas and nodules from South West Uganda. *Mineralogical Magazine*, 44, 315-323.
- MALLMANN, G. & O'NEILL, H. S. C. 2009. The crystal/melt partitioning of V during mantle melting as a function of oxygen fugacity compared with some other elements (Al, P, Ca, Sc, Ti, Cr, Fe, Ga, Y, Zr and Nb). *Journal of Petrology*, 50, 1765-1794.
- MANTON, W. & TATSUMOTO, M. 1971. Some Pb and Sr isotopic measurements on eclogites from the Roberts Victor mine, South Africa. *Earth and Planetary Science Letters*, 10, 217-226.
- MCCLLENAGHAN, B. J. 1989. Letlhakane mine review, De Beers Botswana Mining Company (Pty) Limited. *Internal Report*.
- MCDONOUGH, W. F. & RUDNICK, R. L. 1998. Mineralogy and composition of the upper mantle. *Reviews in mineralogy*, 37, 139-164.
- MCDONOUGH, W. F. & SUN, S.-S. 1995. The composition of the Earth. *Chemical geology*, 120, 223-253.
- MEYER, H. O., TSAI, H. M. & GURNEY, J. J. 1979. A Unique Enstatite Megacryst with Coexisting Cr-Poor and Cr-Rich Garnet, Weltevreden Floors, South Africa. *The Mantle Sample: Inclusion in Kimberlites and Other Volcanics*, 279-291.

- MITCHELL, R. H. 1986. *Kimberlites: mineralogy, geochemistry, and petrology*, Springer Science & Business Media.
- MURAVYEVA, N., BELYATSKY, B., VALERY, S. & IVANOV, A. 2017. *Virunga leucite basanites: Mantle metasomatism or crustal contamination?*
- MURAVYEVA, N. & SENIN, V. 2016. Glimmerite-wehrlite xenolith from the ugandite of East African Rift: Mineral composition and conditions of formation. *Geochemistry International*, 54, 457-463.
- MURAVYEVA, N. & SENIN, V. 2018. Xenoliths from Bunyaruguru volcanic field: Some insights into lithology of East African Rift upper mantle. *Lithos*, 296, 17-36.
- NEUMANN, E.-R., WULFF-PEDERSEN, E., SIMONSEN, S., PEARSON, N., MARTÍ, J. & MITJAVILA, J. 1999. Evidence for fractional crystallization of periodically refilled magma chambers in Tenerife, Canary Islands. *Journal of Petrology*, 40, 1089-1123.
- O'NEILL, C. J. & MORESI, L. 2003. How long can diamonds remain stable in the continental lithosphere? *Earth and Planetary Science Letters*, 213, 43-52.
- POUCLET, A., BELLON, H. & BRAM, K. 2016. The Cenozoic volcanism in the Kivu rift: Assessment of the tectonic setting, geochemistry, and geochronology of the volcanic activity in the South-Kivu and Virunga regions. *Journal of African Earth Sciences*, 121, 219-246.
- PRELEVIĆ, D. & FOLEY, S. 2007. Accretion of arc-oceanic lithospheric mantle in the Mediterranean: evidence from extremely high-Mg olivines and Cr-rich spinel inclusions in lamproites. *Earth and Planetary Science Letters*, 256, 120-135.
- PRELEVIĆ, D., JACOB, D. E. & FOLEY, S. F. 2013. Recycling plus: a new recipe for the formation of Alpine–Himalayan orogenic mantle lithosphere. *Earth and Planetary Science Letters*, 362, 187-197.
- RAWLINSON, P. J. & DAWSON, J. 1979. A Quench Pyroxene-Ilmenite Xenolith from Kimberlite: Implications for Pyroxene-Ilmenite Intergrowths. *The Mantle Sample: Inclusion in Kimberlites and Other Volcanics*, 292-299.
- REED, S. 1965. Characteristic fluorescence corrections in electron-probe microanalysis. *British Journal of Applied Physics*, 16, 913.
- REED, S. J. B. 2005. *Electron microprobe analysis and scanning electron microscopy in geology*, Cambridge University Press.
- ROGERS, N., DE MULDER, M. & HAWKESWORTH, C. 1992. An enriched mantle source for potassic basanites: evidence from Karisimbi volcano, Virunga volcanic province, Rwanda. *Contributions to Mineralogy and Petrology*, 111, 543-556.
- ROSENTHAL, A., FOLEY, S., PEARSON, D. G., NOWELL, G. M. & TAPPE, S. 2009. Petrogenesis of strongly alkaline primitive volcanic rocks at the propagating tip of the western branch of the East African Rift. *Earth and Planetary Science Letters*, 284, 236-248.
- SAUZÉAT, L., RUDNICK, R. L., CHAUVEL, C., GARÇON, M. & TANG, M. 2015. New perspectives on the Li isotopic composition of the upper continental crust and its weathering signature. *Earth and Planetary Science Letters*, 428, 181-192.
- SCOTT, V. & LOVE, G. 1992. Formulation of a universal electron probe microanalysis correction method. *X-Ray Spectrometry*, 21, 27-35.
- SEITZ, H.-M. & WOODLAND, A. B. 2000. The distribution of lithium in peridotitic and pyroxenitic mantle lithologies—an indicator of magmatic and metasomatic processes. *Chemical Geology*, 166, 47-64.
- SØAGER, N., PORTNYAGIN, M., HOERNLE, K., HOLM, P. M., HAUFF, F. & GARBE-SCHÖNBERG, D. 2015. Olivine major and trace element compositions in southern Payenia basalts, Argentina: evidence for pyroxenite–peridotite melt mixing in a back-arc setting. *Journal of Petrology*, 56, 1495-1518.
- SOBOLEV, A. V., HOFMANN, A. W., KUZMIN, D. V., YAXLEY, G. M., ARNDT, N. T., CHUNG, S.-L., DANYUSHEVSKY, L. V., ELLIOTT, T., FREY, F. A. & GARCIA, M.

- O. 2007. The amount of recycled crust in sources of mantle-derived melts. *Science*, 316, 412-417.
- SOBOLEV, A. V., HOFMANN, A. W., SOBOLEV, S. V. & NIKOGOSIAN, I. K. 2005. An olivine-free mantle source of Hawaiian shield basalts. *Nature*, 434, 590-597.
- SOBOLEV, N., LOGVINOVA, A., ZEDGENIZOV, D., POKHILENKO, N., MALYGINA, E., KUZMIN, D. & SOBOLEV, A. 2009. Petrogenetic significance of minor elements in olivines from diamonds and peridotite xenoliths from kimberlites of Yakutia. *Lithos*, 112, 701-713.
- STACHEL, T. & HARRIS, J. W. 2008. The origin of cratonic diamonds — Constraints from mineral inclusions. *Ore Geology Reviews*, 34, 5-32.
- STACHEL, T., VILJOEN, K., MCDADE, P. & HARRIS, J. 2004. Diamondiferous lithospheric roots along the western margin of the Kalahari Craton—the peridotitic inclusion suite in diamonds from Orapa and Jwaneng. *Contributions to Mineralogy and Petrology*, 147, 32-47.
- STAFE, M., NEGUTU, C., PUSCAS, N. N. & POPESCU, I. 2010. Pulsed laser ablation of solids. *Rom. Rep. Phys*, 62, 758-770.
- STIEFENHOFER, J. 1994. The petrography, mineral chemistry and isotope geochemistry of a mantle xenolith suite from the Letlhakane DK 1 and DK 2 kimberlite pipes, Botswana.
- STIEFENHOFER, J., VILJOEN, K. & MARSH, J. 1997. Petrology and geochemistry of peridotite xenoliths from the Letlhakane kimberlites, Botswana. *Contributions to Mineralogy and Petrology*, 127, 147-158.
- STOPPA, F., WOOLLEY, A., LLOYD, F. & EBY, N. 2000. Carbonatite lapilli-bearing tuff and a dolomite carbonatite bomb from Murumuli crater, Katwe volcanic field, Uganda. *Mineralogical Magazine*, 64, 641-650.
- SYLVESTER, P. 2008. Laser Ablation ICP-MS in the Earth Sciences: Current Practices and Outstanding Issues. *Mineralogical Association of Canada, Short Course Volume 40*.
- TAPPE, S., FOLEY, S. & PEARSON, D. 2003. The kamafugites of Uganda: a mineralogical and geochemical comparison with their Italian and Brazilian analogues. *Periodico di Mineralogia*, 72, 51-77.
- THOMAS, R. 2013. *Practical guide to ICP-MS: a tutorial for beginners*, CRC press.
- VETER, M., FOLEY, S. F., MERTZ-KRAUS, R. & GROSCHOPF, N. 2017. Trace elements in olivine of ultramafic lamprophyres controlled by phlogopite-rich mineral assemblages in the mantle source. *Lithos*, 292, 81-95.
- VON KNORRING, O. 1967. Carbonatitic rocks from the volcanic field of western Uganda. *11th Annual Report Institute of Africa geology, University of Leeds*, 30-32.
- WADE, J. A., PLANK, T., MELSON, W. G., SOTO, G. J. & HAURI, E. H. 2006. The volatile content of magmas from Arenal volcano, Costa Rica. *Journal of Volcanology and Geothermal Research*, 157, 94-120.
- WINDOM, K. E. & BOETTCHER, A. 1980. Mantle metasomatism and the Kimberlite-Lamprophyre association: Evidence from an eclogite nodule from Roberts Victor Mine, South Africa. *The Journal of Geology*, 88, 705-712.
- WINTER, J., D 2010. *Principles of Igneous and Metamorphic Petrology*, Pearson.
- WOODLAND, A. & KOCH, M. 2003. Variation in oxygen fugacity with depth in the upper mantle beneath the Kaapvaal craton, Southern Africa. *Earth and Planetary Science Letters*, 214, 295-310.
- WOOLLEY, A. 2001. Alkaline rocks and carbonatites of the world. Part 3: Africa. Geological Society. *Natural History Museum, London*.
- ZHANG, L. Y., PRELEVIĆ, D., LI, N., MERTZ-KRAUS, R. & BUHRE, S. 2016. Variation of olivine composition in the volcanic rocks in the Songliao basin, NE China: lithosphere control on the origin of the K-rich intraplate mafic lavas. *Lithos*, 262, 153-168.



## Appendices

Table 4: Results of external standard and reference material analyses.

BCR-2G		N=17	GeoReM		NIST610		N=32	GeoReM	
Average			Value		Average			Value	
	ppm	2SD	ppm	2SD		ppm	2SD	ppm	2SD
Li	9.74	0.61	9	2	Li	479	32.3	468	24
B	16.9	6.18	6	2	B	203	124	350	56
Na <sub>2</sub> O*	3.24	0.207	3.23	0.14	Na <sub>2</sub> O*	13.6	0.522	13.4	0.3
Al <sub>2</sub> O <sub>3</sub> *	14.6	0.649	13.4	0.8	Al <sub>2</sub> O <sub>3</sub> *	1.91	0.0405	1.95	0.04
P <sub>2</sub> O <sub>5</sub> *	0.318	0.0521	0.37	0.02	P	388	74.5	413	46
CaO*	7.06	0.143	7.06	0.22	CaO*	11.4	0.103	11.4	0.2
Sc	32	1.81	33	4	Sc	383	107	455	10
Ti	15300	1180	14100	2000	Ti	493	35	452	10
V	442	24.2	425	36	V	462	16.9	450	9
Cr	15.5	1.55	17	4	Cr	422	30.7	408	10
Mn	1590	74.1	1550	140	Mn	445	18.7	444	13
Co	39.6	2.64	38	4	Co	420	21.6	410	10
Ni	12.7	1.28	13	4	Ni	460	33.3	459	4
Cu	20.4	11.4	21	10	Cu	451	21.2	441	15
Zn	219	24.2	125	10	Zn	459	23.4	460	18
Ga	73.7	12.5	23	2	Ga	441	18.8	433	13
Sr	330	8.07	342	4	Sr	511	9.59	516	1
Y	29.6	2.27	35	6	Y	464	21.9	462	11
Zr	161	13.7	184	30	Zr	441	28.5	448	9
Nb	12.9	0.591	12.5	2	Nb	465	20.8	465	34
Ba	673	23.5	683	7	Ba	442	16	452	9
La	23.6	0.864	24.7	0.3	La	434	8.62	440	10
Ce	50.8	1.91	53.3	0.5	Ce	452	13.8	453	8
Gd	5.97	0.518	6.71	0.07	Gd	443	12.1	449	12
Yb	3.06	0.333	3.39	0.06	Yb	464	14.6	450	9

Table 3: EMP conditions table

#	Element	Val	Mem	Block	Standard name	Cond.	cps / ppm	Counting times Unk.sec. (Std.sec. * n points)
1	Al Ka	3	1	a	aAl <sub>2</sub> O <sub>3</sub>	20	26500 / 35	Al 160 (10*4)
2	Cr Ka	3	1	a	aCr <sub>2</sub> O <sub>3</sub>	20	23140 / 50	Cr 60(10*4)
3	Fe Ka	2	1	a	aFe <sub>2</sub> O <sub>3</sub>	20	5802 / 144	Fe 20(20*4)
4	Ni Ka	2	1	a	aNiO	20	30140 / 60	Ni 50(10*4)
5	Mn Ka	2	1	a	aRHODONITE	20	2050 / 100	Mn 50(30*5)
6	Ti Ka	4	1	a	aTiO <sub>2</sub>	20	15100 / 90	Ti 50(15*5)
7	V Ka	3	1	a	aV	20	24980 / 100	V 50(10*5)
8	Ca Ka	2	1	a	aWOLLASTONITE	20	10460 / 45	Ca 50(15*4)
9	Co Ka	2	1	b	bCOBALTITE	20	12300 / 35	Co 40(25*5)
10	Mg Ka	4	1	b	bOLIVINE	20	8956 / 144	Mg 15(20*4)
11	Si Ka	4	1	b	bOLIVINE	20	1111 / 170	Si 30(40*5)
Oxide ZAF overlaps: TiK>VK=0.0651 V>Cr=0,1676, FeK $\alpha$ >CoK $\alpha$ =0,00704, CrK $\alpha$ >MnK $\alpha$ =0.000154 Calibration conditions: 20kV, 20nA								

Table 5: Standard deviations EMP olivine analyses in wt% oxide.

	Virunga					Toro-Ankole					Kalahari			
	C-2831	C-2878	C-2797	C-2823	C-2787	C-5619	C-5775	C-6066	C-6098	C-3946	FS1	FS4	RVK1	LK1
Al <sub>2</sub> O <sub>3</sub>	0.00419	0.00586	0.00318	0.00552	0.0185	*	0.00566	0.00984	0.0334	0.00838	0.00509	0.00811	0.00279	0.0237
SiO <sub>2</sub>	0.200	0.159	0.252	0.117	0.538	*	0.162	0.293	0.116	0.0659	0.364	0.130	0.240	0.547
CaO	0.0321	0.0146	0.0396	0.00729	0.0338	*	0.0847	0.0137	0.0393	0.121	0.0184	0.00674	0.00664	0.0264
MnO	0.0178	0.0108	0.0348	0.0162	0.00501	*	0.0183	0.00492	0.00885	0.0396	0.0141	0.00817	0.0209	0.0288
CoO	0.00574	0.00661	0.00212	0.00517	0.00564	*	0.00434	0.00425	0.00471	0.0061	0.00537	0.00439	0.0029	0.00256
MgO	0.612	0.366	1.18	0.478	0.919	*	0.238	0.513	0.333	0.395	1.04	0.253	1.16	1.95
TiO <sub>2</sub>	0.00714	0.00848	0.00907	0.0106	0.00611	*	0.00654	0.00918	0.023	0.00721	0.0150	0.00939	0.00810	0.00784
Cr <sub>2</sub> O <sub>3</sub>	0.00449	0.00554	0.00623	0.00857	0.0107	*	0.00784	0.0106	0.00878	0.00868	0.00458	0.00982	0.00630	0.0109
FeO	0.770	0.352	1.24	0.419	0.514	*	0.263	0.737	0.402	0.429	1.35	0.452	1.54	2.79
NiO	0.00332	0.00415	0.00726	0.00275	0.0431	*	0.0382	0.0154	0.00999	0.0752	0.0263	0.0311	0.0226	0.0892
V <sub>2</sub> O <sub>3</sub>	0.00212	0.00449	0.00259	0.00889	0.00303	*	0.00427	0.00206	0.00712	0.00839	0.00557	0.00191	0.00375	0.00644
Total	0.207	0.164	0.158	0.224	0.128	*	0.357	0.374	0.164	0.241	0.186	0.303	0.334	0.414
Mg#	0.964	0.452	1.67	0.542	0.631	*	0.268	0.772	0.429	0.467	1.43	0.462	1.62	2.97

Table 6: Standard deviations LA-ICP-MS olivine analyses in ppm.

	Virunga					Toro-Ankole					Kalahari			
	C2831	C2878	C2797	C2823	C2787	C5619	C5775	C6066	C6098	C3946	FS1	FS4	RVK1	LK1
Li	0.730	0.407	0.441	0.415	0.161	*	0.145	0.374	0.158	0.117	0.468	0.171	0.510	0.431
B	0.515	0.546	0.170	5.01	0.635	*	1.46	0.870	0.409	0.837	2.47	1.43	3.31	0.736
Na	7.32	5.54	6.59	3.30	12.0	*	6.09	31.6	51.7	4.27	42.9	31.4	20.4	84.2
Al	6.76	4.09	9.86	6.63	40.6	*	4.00	18.6	11.9	12.2	31.3	25.2	6.29	56.5
P	58.0	46.4	29.0	14.1	14.5	*	8.29	5.51	12.2	3.97	27.9	3.89	18.8	21.5
Ca	168	73.0	187	120	129	*	365	84.9	182	187	86.4	67.8	27.3	119
Sc	0.165	0.145	0.0887	0.269	0.240	*	0.833	0.0953	0.362	0.136	0.248	0.372	0.358	0.227
Ti	28.5	44.3	51.5	9.45	6.73	*	14.6	20.2	37.8	5.33	48.2	8.95	32.1	24.2
V	0.200	1.51	0.687	0.428	0.490	*	0.560	2.18	3.07	0.416	2.72	1.61	0.864	4.27
Cr	7.13	5.85	8.89	7.06	59.7	*	20.7	102	100	112	41.0	71.8	46.7	85.2
Mn	148	123	249	95.0	78.3	*	115	23.9	55.6	83.8	141	87.0	189	298
Co	3.01	6.65	4.15	8.45	4.43	*	7.26	7.27	4.86	1.90	16.7	5.43	14.7	14.9
Ni	8.01	20.2	20.3	32.3	361	*	278	132	106	181	318	208	190	773
Cu	0.0785	0.0635	0.112	0.174	0.755	*	0.469	1.75	2.84	0.261	1.85	2.07	0.430	3.05
Zn	6.80	7.54	7.26	6.55	4.85	*	4.31	11.7	7.51	2.26	20.3	8.6	14.5	34.6
Ga	0.0152	0.00995	0.0198	0.0121	0.0303	*	0.0357	0.0353	0.0394	0.0476	0.0871	0.0381	0.0249	0.130
Sr	0.00832	0.0142	0.00982	0.00511	0.00704	*	0.00698	0.00675	0.0173	0.00765	0.00261	0.000867	0.00724	0.00891
Y	0.0331	0.0227	0.0701	0.00775	0.00407	*	0.0296	0.00464	0.00911	0.00948	0.0809	0.00264	0.00124	0.00472
Zr	0.158	0.032	0.0378	0.0119	0.177	*	0.123	0.182	0.186	0.00758	0.0797	0.0442	0.0472	0.202
Nb	0.00669	0.00935	0.0132	0.00094	0.00218	*	0.00228	0.000597	0.00704	0.00493	0.0781	0.0363	0.0570	0.147
Ba	0.0245	0.00567	0.0219	0.00484	0.0310	*	0.0086	0.00282	0.00212	0.0139	0.00557	0.00472	0.00858	0.00265
La	0.0241	0.0152	0.0338	0.0131	0.0313	*	0.00442	0.0173	0.0375	0.00130	0.00355	0.000585	0.00106	0.000521
Ce	0.319	0.185	0.472	0.0212	0.304	*	0.0435	0.00518	0.0687	0.00301	0.0435	0.00176	0.00267	0.00143
Gd	0.00574	0.0033	0.00672	0.00268	0.0124	*	0.00332	0.00113	0.00215	0.00452	0.00554	0.00203	0.00576	0.00367
Yb	0.0185	0.00952	0.0254	0.00703	0.00304	*	0.0185	0.00121	0.00159	0.00853	0.0429	0.00086	0.00264	0.00247

\*= only one grain sampled